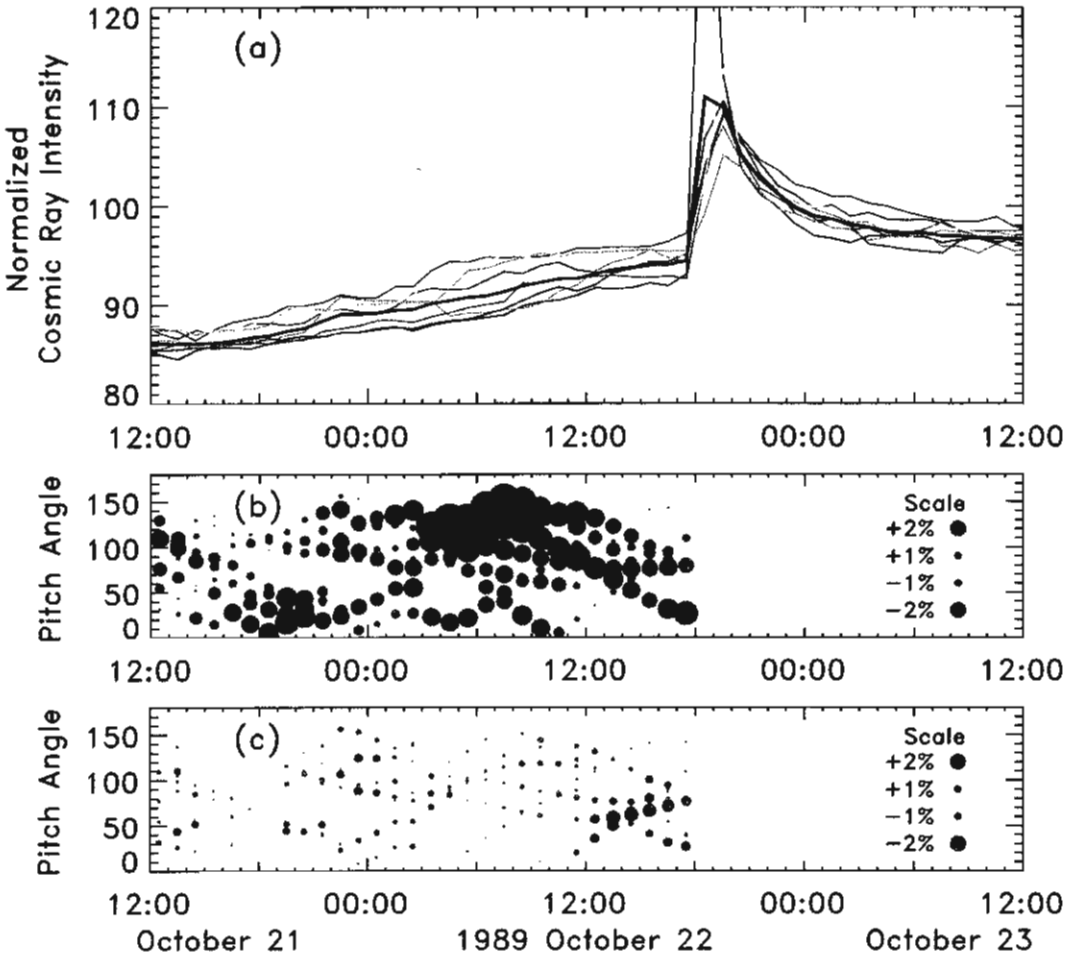

FIG. 4.—(*a*) Average hourly counting rate for eight sea-level polar neutron monitors (*colored lines*) along with the omnidirectional average (*heavy black line*) from 1989 October 21, 12:00 UT to October 23, 12:00 UT. (*b*) Anisotropy of GCRs before the GLE onset, where the radius of a green (red) circle indicates the positive (negative) percentage deviation from the average in (*a*). (*c*) Bidirectional anisotropy, the residual when subtracting a dipole anisotropy from (*b*), is associated with a closed magnetic loop configuration.

100°, indicating that stations viewing anti-sunward relative to the nominal spiral observed intensities more than 2% above the mean, while stations with small pitch angles observed intensities about 2% below the mean. Presumably this strong unidirectional anisotropy occurs because GCRs are refilling the inner heliosphere during the recovery phase of the Forbush decrease, following departure of the CME ejecta.

Figure 4*c* is similar to Figure 4*b*, except that here the dipole anisotropy (or first-order anisotropy) has been subtracted from the data. The residual after subtraction then represents higher order anisotropies present in the data. The important feature of Figure 4*c* is that there is noticeable bidirectional anisotropy after 12:00 UT on October 22, just before the GLE onset. The characteristic feature of bidirectional flow is that intensities are suppressed near 90° pitch angle and are elevated at both 0° and 180°. In the figure this is evidenced by comparatively large red circles (suppressed intensity) in the middle of the plot, with green circles (elevated intensity) on either side. The bidirectional flow is quite strong in comparison with the low or undetectable bidirectional anisotropy generally found in undisturbed interplanetary conditions.

Richardson et al. (2000) have shown that such bidirectional flows of GCRs are associated with a magnetic loop configuration. CMEs and their interplanetary ejecta are known to often remain magnetically connected to the Sun by large-scale closed magnetic loops. Because the actual ejecta, as defined by physical properties of the plasma such as a depressed proton temperature (Richardson & Cane 1993), have a limited radial extent, the "legs" of closed magnetic loops that connect back to the Sun must include substantial regions of more normal plasma that does not bear the physical signatures of ejecta. (Unfortunately, plasma data from the *Interplanetary Monitoring Platform 8* spacecraft, which indicated the presence of ejecta up to the start of October 22, were unavailable thereafter; see Richardson et al. 2000.) Thus the bidirectional anisotropy of GCRs preceding the GLE of October 22 is best explained if the Earth was inside a closed magnetic loop configuration, although perhaps not inside the ejecta from the October 19 event but instead in one leg connecting back to the Sun.

2.3. *Relativistic Solar Protons*

To analyze the distribution of relativistic solar protons, the total count rate from each polar neutron monitor was corrected for atmospheric pressure variations using separate absorption lengths for Galactic and solar particles. For the latter we adopt a value of 100 g cm^{-2} as generally found in prior studies (Duggal 1979). Data from all stations were formatted to a common cadence of 5 minutes and corrected to a common standard pressure

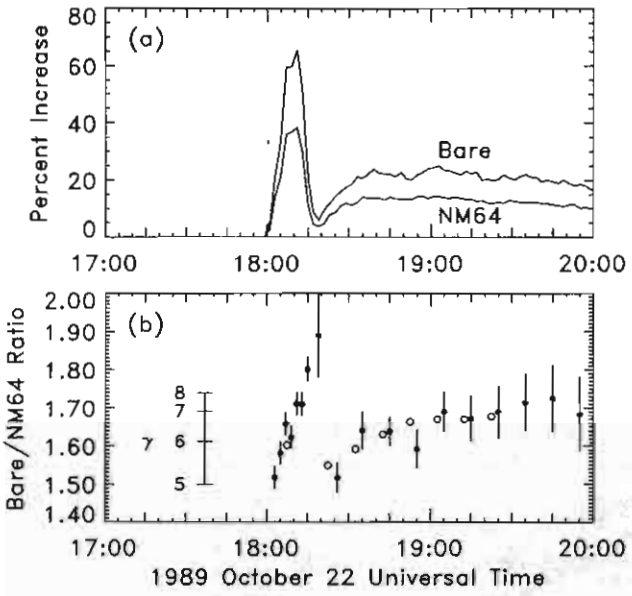

FIG. 5.—(*a*) Percent increases recorded at the South Pole by a standard (NM64) neutron monitor and a Polar Bare neutron counter that lacks the usual lead shielding. (*b*) Ratio of percent increases (*filled circles*), which provides an indication of spectral index γ. The variations at onset reflect the sequence of dispersive onset and exit of the spike and dispersive onset of the hump. Spectral indices of Cramp et al. (1997) for 5 minute intervals are shown for comparison (*open circles*).

of 760 mm Hg. We thereby obtain the percentage increase of each counting rate over the GCR background, which was modeled by fitting a linear trend to the hourly density (Fig. 4*a*, *heavy dark line*) over the interval 00:00–18:00 UT on October 22.

Information on the spectrum of relativistic solar protons was obtained by comparing the count rate of the South Pole neutron monitor with the count rate of a nearby "Polar Bare" set of neutron counters that lack the usual lead shielding of a standard NM64 detector system (Bieber & Evenson 1991). The count rates and their ratio are shown in Figure 5. As shown in the top panel, the Polar Bare is relatively more sensitive to low-energy primaries, and it records a higher percentage increase than the standard NM64 owing to the soft spectrum of solar cosmic rays. With the aid of yield functions provided by Stoker (1985), the Bare/NM64 ratio can be translated into a spectral index. We assume a differential rigidity spectrum of power-law form ($P^{-\gamma}$ with P the rigidity and γ the spectral index) with an upper cutoff at 20 GV. The inset scale on the left side of the lower panel shows the spectral index implied by the corresponding Bare/NM64 ratio. Error bars include both a random component and a systematic component from the uncertainty of the Galactic background. In addition, during the spike there could be a small systematic error of up to 0.6 in the spectral index estimate, due to the strong anisotropy and the different Bare and NM64 asymptotic directions (Bieber & Evenson 1991; Cramp et al. 1997).

For comparison, the results from the previous analysis of Cramp et al. (1997) using data from neutron monitors at different cutoff rigidities are shown by open circles. Each open circle indicates an estimate for a 5 minute interval. The overall agreement is remarkable, and it improves our confidence in both techniques.

The dramatic variations in γ with time at the start of the GLE are correlated with changes in the particle flux. They are due to rigidity dispersion during the onset of the spike, end of the spike, and onset of the hump. For example, as the "spike" of particles arrives from the Sun, faster particles arrive first, so there is a lower spectral index while the flux rises. When this pulse of particles passes beyond Earth, the faster particles leave first, resulting in a higher spectral index when the flux declines. Since the time variation in the spectrum of particles arriving at the Earth is qualitatively explained by such dispersion effects, the spectrum injected at the Sun may well be constant, and is assumed so for simplicity. We adopt a spectral index of 5.9 for the solar proton spectrum. This implies that the median rigidity detected by a polar neutron monitor is 1.6 GV, and the central 50% of the detector response is for ions of 1.1–2.3 GV.

As discussed in § 2.1, the time profiles of nine polar neutron monitors directly provide the time-dependent distribution of particles in nine viewing directions. This information on the directional distribution is to be compared with transport modeling of the distribution of particles in time, position, momentum, and pitch angle. To do so, we need to assign a pitch angle to the viewing direction of each neutron monitor. For particles of much lower energy, the pitch angle could safely be defined with respect to the local magnetic field. However, there is a gap in measurements of the solar wind speed and magnetic field in the OMNI database maintained by the US National Space Science Data Center between 1989 October 22, 02:00 UT and October 26, 18:00 UT (see Fig. 1 of Cane & Richardson 1995). Furthermore, it should be noted that a 2 GV proton has a Larmor radius of about 0.01 AU, on the same order as the coherence length of interplanetary magnetic turbulence (≈0.02 AU), so it is not clear that the particle orbits should be organized around the instantaneous magnetic field measured at the point of observation. In practice, energetic particles in interplanetary space are typically found to exhibit distributions with an axis of symmetry, and Bieber & Evenson (1987) showed that even for ~50 MeV protons, the axis of symmetry fluctuates randomly about the measured field direction. Therefore, a standard approach is to find an empirical axis of symmetry and to define the pitch angle with respect to that for a comparison with the transport modeling.

It is clear that an interpretation of the directional distribution of energetic particles requires some modeling, at least to determine the axis of symmetry. Furthermore, it would be difficult to fit the station data directly, as they have correlated uncertainties in the pitch angle, an independent variable, due to the uncertain axis of symmetry. Therefore, we characterize the directional distribution in terms of the omnidirectional average intensity or "density" n and the weighted anisotropy s (product of density and dipole anisotropy, also the first-order Legendre coefficient). In terms of the cosmic-ray directional intensity, $f(\mu)$, the density and weighted anisotropy are defined as

$$n = \frac{1}{2}\int_{-1}^{+1} f(\mu)\, d\mu, \tag{1a}$$

$$s = \frac{3}{2}\int_{-1}^{+1} \mu f(\mu)\, d\mu, \tag{1b}$$

where μ is pitch-angle cosine relative to the axis of symmetry. The quantities n and s have the same units as $f(\mu)$, which in the analysis of GLEs is often expressed as a "percent increase" relative to the pre-event Galactic background. Throughout this article, we refer to n as the "density" because it has the same time profile as the true density up to a constant scaling factor. Note that the ordinary dipole anisotropy ξ can be expressed in terms of n and s as $\xi = s/n$. In model refinements in § 4.2, we also fit the curvature of the pitch-angle distribution, defined as the second-order Legendre coefficient.

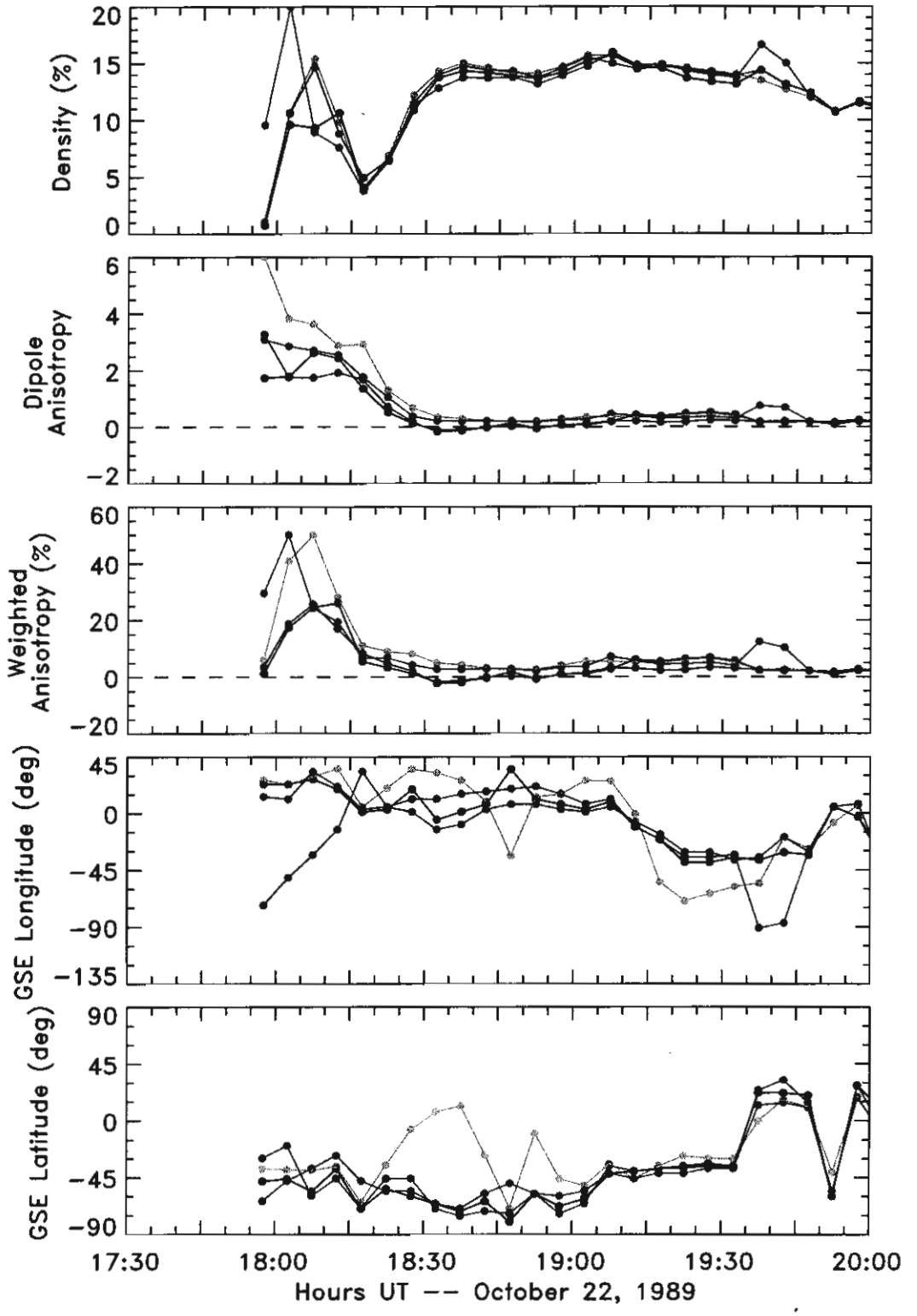

FIG. 6.—Density, dipole anisotropy, and weighted anisotropy of relativistic solar protons and GSE longitude and latitude of the axis of symmetry as derived from fits to directional information from nine polar neutron monitors for four models of the pitch-angle distribution: a first-order Legendre polynomial (*green*), exponential plus constant (*blue*), second-order Legendre polynomial (*red*), and two exponentials plus constant (*black*). The average values of the density and weighted anisotropy, expressed as the percent increase over the Galactic background, is then fit to evaluate the candidate magnetic field configurations.

Figure 6 shows the density, dipole anisotropy, weighted anisotropy, and GSE longitude and latitude of the axis of symmetry for fits to four models of the pitch-angle distribution at each time:

$$f(\mu) = a_0 + a_1\mu, \tag{2a}$$

$$f(\mu) = a_0 + a_1 \exp(b\mu), \tag{2b}$$

$$f(\mu) = a_0 + a_1\mu + a_2\left(\frac{3}{2}\mu^2 - \frac{1}{2}\right), \tag{2c}$$

$$f(\mu) = a_0 + a_1 \exp(b\mu) + a_2 \exp(-b\mu), \tag{2d}$$

where $\{a_i\}$ and b are fit parameters. These represent, respectively, a first-order Legendre polynomial, exponential plus constant, second-order Legendre polynomial, and two exponentials plus constant. The latter two are expected to provide better fits to bidirectional fluxes. Note that for equations (2*a*) and (2*c*), a_0 and a_1 are directly interpreted as n and s, respectively, whereas for equations (2*b*) and (2*d*), n and s must be computed by performing the integrals in equations (1*a*) and (1*b*).

Our results for the axis of symmetry are reasonably consistent with those derived by Cramp et al. (1997) for neutron monitors with a variety of cutoff rigidities. With the exception of the spike period of 17:55–18:10 UT (to be discussed shortly), results for our four models are reasonably similar for the density and weighted anisotropy, which are then taken as data to be fit to determine the optimal transport model and injection function of relativistic solar protons. For 18:10–19:30 UT, the fitting in § 4.1 uses the average density and weighted anisotropy for these four models. The standard deviation among the four models over 18:15–19:30 was used to estimate the uncertainty in the density and weighted anisotropy data for these time intervals. The uncertainties for 18:10–18:15 are evidently greater and were estimated from the standard deviation among the four fits for this single 5 minute interval. At 19:30 there is an abrupt change in the axis of symmetry. Note that as the weighted anisotropy becomes smaller, the inferred axis of symmetry tends to fluctuate substantially.

We do not mean to imply that the directional distribution is completely described by specifying the density and weighted anisotropy, or indeed by the model functions we have chosen. The reason for extracting the density and weighted anisotropy is that, in practice, these two quantities adequately discriminate between correct and incorrect scenarios of interplanetary transport. (For example, the anisotropy can constrain the mean free path of interplanetary scattering.) As a check, we take the transport model and injection function that best fit the density and weighted anisotropy profiles and examine the complete pitch-angle distribution produced by the model, in comparison with the pitch angle and count rate at individual stations for various time intervals. In previous analyses for other GLEs, we have found that models that fit the density and weighted anisotropy profiles generally also provide an adequate representation of the observed pitch-angle distributions (Bieber et al. 2002, 2004a).

During the time of the initial spike with high anisotropy, 17:55–18:10 UT, only two neutron monitor stations, MC and SP, registered a noticeable increase in count rate (see Fig. 2). This is a special case where the directional distribution is so narrow that a large portion could fall in the "holes" in our directional coverage (see Fig. 3). This is why the density and weighted anisotropy estimates vary so widely among the four models. For this time period, we therefore determine lower limit values for the density and weighted anisotropy by fitting the station data to an exponential function of the pitch-angle cosine, subject to the constraint that McMurdo station was forced to have a pitch angle of 0°. This procedure provides a valid lower limit, because the exponential function is monotonic and because McMurdo observed the largest increase of all the stations during this interval. Any fit with McMurdo at nonzero pitch angle would necessarily yield a higher density and weighted anisotropy than the fit with McMurdo at 0°. These lower limits are enforced when fitting time profiles.

3. MODELING OF TRANSPORT AND INJECTION

3.1. *Interplanetary Transport*

This section describes how we fit the density and anisotropy profiles extracted from these nine polar neutron monitors by simulating the interplanetary transport of solar protons and then determining the optimal injection function near the Sun for each magnetic field model. We first solve a transport equation that takes into account pitch-angle scattering and adiabatic focusing (Ruffolo 1991) using the numerical method of Nutaro et al. (2001). The interplanetary transport of charged particles can also be affected by solar wind convection and adiabatic deceleration (Ruffolo 1995). We could neglect these processes in comparison with scattering and focusing because the solar wind speed is much slower than the speed of relativistic particles (by a factor of ≈500). Similarly, we could neglect the Compton-Getting transformation (Compton & Getting 1935) of the pitch-angle distribution from the solar wind frame, in which it is calculated, into the Earth's reference frame, which has a negligible effect on the anisotropy for the relativistic particles considered here. In our simulations we include these effects for spiral and bottleneck configurations, but neglect them for the loop configuration to avoid specifying the precise shape of the magnetic field line as would be required to properly describe those minor effects. We note that the present numerical method can reproduce the results of Ruffolo (1995), which have also been reproduced by independent numerical techniques (Hatzky et al. 1997; Lario et al. 1998; Kocharov et al. 1998).

The transport equation governs the time evolution of the particle distribution function $F(t, \mu, z, p)$, where t is time, μ is the pitch-angle cosine, which determines the velocity component along the magnetic field, $v_z = \mu v$, z is the arclength along a magnetic field line from the Sun, and p is the particle momentum.

In other words, we determine the directional distribution of particles at all locations along the local magnetic field line, as a function of time and for each rigidity (momentum) of interest. The initial condition is that particles are initially close to the Sun, corresponding to an instantaneous injection. The simulation results are then convolved with an injection function (see § 1.2), i.e., a time profile of particle release near the Sun. The particles are taken to be protons. In reality the neutron monitor responds to any primary cosmic-ray ions with a rigidity-dependent yield function, and there is a small admixture of other ions in SEPs. However, the interplanetary scattering mean free path is commonly viewed to be a function of rigidity alone, and velocity dispersion is a minor effect at relativistic energies, so viewing GLE ions of a given rigidity to be protons does not have a major effect on the transport calculation. In order to represent the momentum distribution of the primary relativistic protons to which the neutron monitors are responding, we perform simulations for momentum values corresponding to the 5th, 15th, . . . , 95th percentile rigidities for the spectral index of 5.9. Results for these 10 momentum values are averaged to determine the density, weighted anisotropy, and curvature expected near the Earth. For the pitch-angle scattering coefficient, we use the standard parameterization $A|\mu|^{q-1}(1 - \mu 2)$ and relate A to the scattering mean free path λ as described by Ruffolo (1991). In the context of standard quasilinear theory, q is identified with the spectral index of the power

spectrum of interplanetary turbulence (Jokipii 1971). We initially use a value of $q = 1.5$, which was found to provide a good fit to the GLE of 2000 July 14 (Bieber et al. 2002). This is also in the range of 1.3–1.7 inferred by Bieber et al. (1986) for lower energy particles. On the other hand, the value of $q = 1.0$ provided a better fit than $q = 1.5$ for pitch-angle distributions measured during the GLE of 2001 April 15 (Bieber et al. 2004a). In refinements to the fits (§ 4.2) we allow this parameter to vary.

In this analysis, we consider three types of magnetic field configurations, corresponding to different ideas as discussed in § 1. These configurations are illustrated in Figure 7. Note that the key transport processes are scattering and focusing, and while scattering depends on small-scale, turbulent magnetic fluctuations, focusing depends on the large-scale magnetic field configuration. The strength of focusing is proportional to $1/L$, defined by

$$\frac{1}{L} \equiv -\frac{1}{B}\frac{dB}{dz}, \tag{3}$$

where L is called the focusing length. Therefore, the key property of each magnetic field configuration, in terms of the particle transport, is the dependence of $1/L$ on z, the distance along the magnetic field from the Sun. The magnetic field configurations are as follows:

1. The standard Archimedean spiral configuration (Parker 1958) for open field lines carried out by the solar wind (Fig. 7*a*). The inverse focusing length is given by

$$\frac{1}{L} = \frac{R(r^2 + 2R^2)}{r(r^2 + R^2)^{3/2}}, \tag{4}$$

where $R = v_{sw}/(\Omega \cos\theta)$, Ω is the sidereal angular frequency of solar rotation (derived from a synodic period of 26.75 days; Bai 1987), and θ is the Earth's heliolatitude (with respect to the solar equator) or 5° N for this event. For the solar wind speed, we adopt the value of 600 km s^{-1} after the data gap in solar wind and magnetic field measurements (1989 October 26 at 18:00 UT) as characteristic of the fast solar wind speed throughout late October. (The value of ≈800 km s^{-1} preceding the data gap, near the start of October 22, was temporarily elevated due to the CME passage around that time.) We therefore estimate R to be 1.38 AU. In this magnetic field configuration, the only free parameter is the radial mean free path, λ_r. Previous authors suggest that it is realistic to take λ_r to be constant in position (Palmer 1982; Beeck et al. 1987; Kallenrode et al. 1992; for a comparison with constant-$\lambda_{\|}$ fitting, see Ruffolo et al. 1998). Note that the parallel mean free path is given by $\lambda_{\|} = \lambda_r/\cos^2\psi$, where ψ is the "garden hose" angle between the field line and the radial direction, given by $\cos\psi = R/(r^2 + R^2)^{1/2}$. Thus in this model $\lambda_{\|}$ varies with position, and at Earth ($r = 0.995$ AU) we have $\lambda_{\|} = 1.52\lambda_r$.

2. A magnetic bottleneck beyond Earth (Fig. 7*b*). Such a configuration provided a good fit to polar neutron monitor data for the 2000 July 14 GLE (Bieber et al. 2002). The local field line is still taken to follow an Archimedean spiral. The difference is that we now consider a compression in ($\ln B$) of Gaussian form

$$\ln B = (\ln B)_{\rm Arch} + \eta \exp\left[-\frac{(r - r_b)^2}{2\sigma^2}\right],$$

$$\frac{1}{L} = -\frac{d}{dz}\ln B = \left(\frac{1}{L}\right)_{\rm Arch} + \eta\cos\psi\frac{r - r_b}{\sigma^2}\exp\left[-\frac{(r - r_b)^2}{2\sigma^2}\right], \tag{5}$$

where "Arch" refers to values for an uncompressed Archimedean spiral field, r_b is the heliocentric distance at the center of the

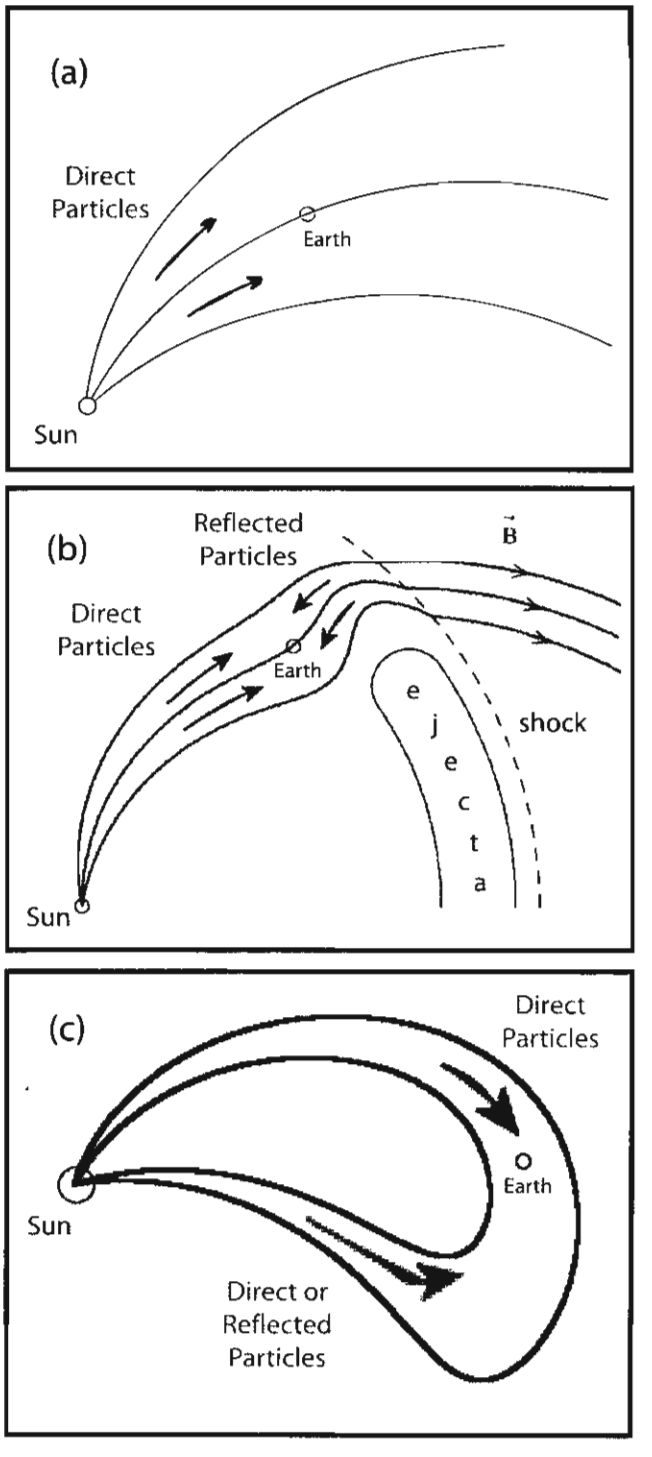

FIG. 7.—Three magnetic field configurations considered in this work: (*a*) standard Archimedean spiral, (*b*) magnetic bottleneck beyond Earth, and (*c*) closed interplanetary magnetic loop, injecting particles along the near leg of the loop that undergo reflection in the far leg, or injecting particles along both legs of the loop. Configurations *b* and *c* could be caused by a previous CME. The only case that provides a good fit to the data is injection along both legs of a closed interplanetary magnetic loop.

bottleneck, σ is a measure of the width of the bottleneck, taken to be 0.05 AU, and the amplitude η is chosen so that the discrete sum of focusing occurring at each grid point corresponds to the desired reflection coefficient (RC) for an isotropic distribution. Thus the free parameters are λ_r, r_b, and RC.

3. A closed interplanetary magnetic loop (Fig. 7*c*). Note that as discussed above, there is no need to specify the detailed shape of the loop, e.g., it could be coiled as in a magnetic cloud. The physical requirements for a loop of length l are

$$\frac{1}{L} \approx \frac{2}{z} \quad \text{as } z \to 0, \tag{6}$$

$$\frac{1}{L} \approx -\frac{2}{l-z} \quad \text{as } z \to l, \tag{7}$$

to be consistent with a nearly radial field near the Sun, and

$$\frac{dB}{dz} = 0 \quad \text{and} \quad \frac{1}{L} = 0 \quad \text{for } z = \frac{l}{2} \tag{8}$$

for symmetry. We satisfy these requirements with the function

$$\frac{1}{L} = \frac{2\pi}{l} \cot\left(\frac{\pi z}{l}\right). \tag{9}$$

Since the cross-sectional area of the loop A is inversely proportional to B, we have $1/L = (dA/dz)/A$ and $A \propto \sin^2(\pi z/l)$. In order to avoid further constraining the shape of the field line, we do not relate the distance z along the loop to the radius r. Therefore, we use the parallel mean free path $\lambda_\parallel$, taken to be constant for simplicity, and the free parameters for this configuration are $\lambda_\parallel$ and l. (We also tried varying the distance along the field from the Sun to the observer, z_{obs}). We have considered injection along either one leg of the loop or both legs of the loop.

Note that the bottleneck and loop configurations would correspond to disturbances by a previous CME. Indeed, as discussed earlier, a flare/CME event from the same active region on 1989 October 19 produced a large GLE and has also been associated with a CME-driven shock that arrived at Earth on October 20 at ≈17:00 UT and the subsequent Forbush decrease in GCRs (Cane & Richardson 1995). That Forbush decrease persisted until the onset of the October 22 GLE, and in § 2.2 we showed bidirectional anisotropies in GCRs that support the model of a loop configuration at the time of GLE onset. Thus there was a major CME-related disturbance of the interplanetary medium shortly before the October 22 GLE, which could have either distorted the fields as in the bottleneck scenario or enveloped the Earth in a magnetic loop, perhaps in one of the legs of nearly radial magnetic field connecting the CME back to the Sun.

3.2. *Fitting to Time Profiles of Density and Anisotropy*

For a given magnetic field configuration and transport model parameters, we simultaneously fit the time profiles of density and weighted anisotropy to determine the optimal piecewise linear injection function. In model refinements (§ 4.2) we simultaneously fit the curvature, as well as another type of anisotropy. The injection function is defined as the rate at which particles are injected at a solar footpoint of the Sun-Earth magnetic field line as a function of time. We evaluate the goodness of fit with a χ^2 statistic and thereby determine the optimal transport parameters and magnetic field configuration. Bieber et al. (2002) compared results for the GLE of 2000 July 14 from this procedure with independent simulation and fitting techniques, and found close agreement.

The estimation of the injection function is a type of inversion problem, in which the data measured at Earth are the known "response" of the transport process. The response is viewed as a convolution between a Green's function for an instantaneous (δ-function) injection, which we determine by the transport simulations described above, and the injection function. The inversion problem is to determine a best-fit injection function, and we should remark on the general requirements for this fitting procedure. The convolution is only valid if the conditions of interplanetary transport are independent of time. This is not valid when the data are strongly affected by transient changes in local interplanetary conditions. In data with multiple energy channels, local transients can often be identified as affecting all channels simultaneously, while transport effects tend to be energy dispersive. For example, the spectral variations for the 1989 October 22 GLE at spike onset and hump onset (Fig. 5) indicate energy-dispersive transport effects. At lower energies, the time profiles of 24–210 MeV SEP proton density presented by Nemzek et al. (1994) are dominated by a sudden, nondispersive decline in various energy channels (see further discussion in § 5). Such profiles are not amenable to the present type of analysis.

Furthermore, the source location is taken to be fixed, a good approximation only so long as the source remains near the Sun. For gradual flare/CME events, there is strong evidence that escaping SEP ions of moderate energy are not produced deep inside the solar corona, but rather are accelerated at traveling CME-driven shocks (Mason et al. 1984; Lee & Ryan 1986; Reames 1990; Ruffolo 1997). Therefore, when we fit data for gradual events, which include all GLEs, a check on the validity of the method is that the resulting injection function should be of sufficiently short duration that the shock was still near the Sun. High-energy SEPs such as those considered in the present work are generally injected quite close to the Sun (e.g., Cliver et al. 2004). This condition can be invalid for low-energy SEP ions from gradual events, which can be continuously accelerated throughout the motion of the shock from the Sun to Earth.

In practice, the transport involves random processes that spread out the distribution, so one can determine at best a small number of injection parameters. A piecewise linear injection function is chosen to provide a flexible shape for the injection function and for computational efficiency. The fit parameters are the injection amplitudes $\{a_i\}$ at joint times $t_i = t_0 + 2^{i-1}\tau$. The number of joint times, amplitudes, and uncertainties are determined by linear least-squares fitting (Ruffolo et al. 1998) for a grid of trial values t_0 and τ.

A special consideration in fitting the density and weighted anisotropy as a function of time on 1989 October 22 is that for three data intervals (17:55–18:10 UT) during the density spike only lower limits are available for these quantities. We also enforce a minimum dipole anisotropy of 2.0, as suggested by the data in Figure 6. Each of these limits was enforced after the least-squares fitting to other data points by adding a penalty of 10^5 to the χ^2 value when the limit was violated. One problem with using lower limits that only partially constrain the onset is that the fit may "cheat" by injecting the particles too early. We therefore padded the data with three intervals of zero values before the spike period, assigning uncertainties as for later times, which serve to prevent a premature onset. For the initial analysis of § 4.1, only joint times before 18:12 UT are considered.

4. RESULTS

4.1. *Magnetic Field Configuration*

In our initial analysis, we fit the average of the density and weighted anisotropy profiles shown in Figure 6 to find a magnetic field configuration and transport parameters that can explain five special features of the 1989 October 22 GLE:

1. The strongly anisotropic spike in density of very short duration, from 17:55 to 18:15 UT.
2. The dip in density to a low value at 18:15–18:20 UT.
3. The rapid onset of a large hump in density at 18:20–18:30 UT.
4. The weighted anisotropy near zero at hump onset, which actually corresponds to bidirectional flows (Cramp et al. 1997).
5. The very slow decay of the hump.

To address these key features, this part of the analysis is limited to data before 19:30 UT. For a manageable optimization problem, we fix various quantities that are not directly relevant to the magnetic configuration. For example, we fix the value of q to 1.5 (see § 3.1), as this mainly affects the detailed pitch-angle distribution, and allow this to vary in refined fits in the next section. We do not fit the curvature of the pitch-angle distribution in this section, as that information is mainly relevant to constraining q.

Figures 8 and 9 show the simulation results for an instantaneous injection near the Sun, as well as the fit to the data after convolution with the best-fit injection function. The various panels are for the best-fit transport parameters for different magnetic field configurations, or for the case of a closed magnetic loop, for injection along one or both legs. The simulated profiles in Figure 8 are summed over the 10 percentile rigidity values used to represent the neutron monitor response (§ 3.1), giving rise to the artificial multiple peak structure within the spike. The profiles could be smoothed by simulating for a larger number of percentile rigidity values, but the data for this event are in 5 minute intervals and the injection has a duration of several minutes, so the present simulations provide sufficiently smooth fit profiles to analyze these data. In all cases the simulation results (Fig. 8) are in units of protons cm ^{2} sr^{-1} s^{-1} MeV^{-1} per injection of 10^{28} protons MV^{-1} per unit solid angle in solar latitude and longitude, and the fits and data (Fig. 9) are expressed as a percentage of the GCR background flux at the start of the GLE. Table 1 provides the χ^2 values, degrees of freedom, and best-fit transport parameters.

The first configuration is an Archimedean spiral magnetic field (Parker 1958; see Fig. 7*a*), which applies in the undisturbed solar wind, allowing the possibility of multiple injections (Shea & Smart 1997). The strong anisotropy of the spike requires a long mean free path, for which a highly anisotropic distribution passes by the detector leaving nearly no density at late times (Figs. 8*a* and 8*b*). Even when convolved with an extended injection function, this model is unable to explain the hump of high density and nearly zero weighted anisotropy (Figs. 9*a* and 9*b*), yielding a high χ^2 value.

The second configuration is a magnetic bottleneck beyond Earth (Fig. 7*b*), as inferred for the GLE of 2000 July 14 (Bieber et al. 2002), which is similar to the suggestion of Cramp et al. (1997) that a fraction of the particles were reflected back by a region of enhanced scattering beyond Earth. Physically the reflection coefficient (RC) cannot be greater than one. This model has trouble producing enough backscattering to account for the strong density in the hump, favoring the maximum RC value of 0.99 with a very large density and weighted anisotropy in the spike (not ruled out by our data, which are lower limits at those times). Note that the reflection coefficient RC is formally defined for an isotropic distribution; for the anisotropic distribution of an outgoing coherent pulse, particles are preferentially in the loss cone near zero pitch angle and the reflection is actually less than RC. Assuming conservation of the magnetic moment, we have $RC = (1 - B_0/B_b)^{1/2}$, where B_b/B_0 is the magnetic field enhancement at the bottleneck, so RC = 0.99 implies $B_b/B_0 \approx 50$, an unreasonably large value. We consider that the optimal fit for RC = 0.99 may instead indicate a completely reflecting configuration such as a loop. For a physically reasonable bottleneck, we restrict the bottleneck configuration to RC $\leq$ 0.95 or a magnetic field enhancement of $B_b/B_0 < 10.2$. The fits again favor the maximum value, RC = 0.95, with results as shown in Figures 8*c*, 8*d*, 9*c*, and 9*d*. The χ^2 value at RC = 0.95 is over twice that for RC = 0.99 (see Table 1), mainly because the leakage of particles through the bottleneck leads to an excessively fast density decline. These results suggest trying a closed magnetic loop configuration in which particles can be trapped, at least in terms of transport parallel to the mean field.

Next we consider a closed interplanetary magnetic loop, as indicated by the bottleneck fitting and bidirectional anisotropy of relativistic solar protons, as well as the bidirectional anisotropy of GCRs prior to the GLE (§ 2.2). We initially thought in terms of injection along one leg of the loop, with the hump due to focusing (mirroring) of particles by the converging magnetic field lines near the solar footpoint of the far leg (see Fig. 7*c*). To our surprise, the fits clearly distinguished this configuration from a perfectly reflecting bottleneck. The difference is that the bottleneck changes the pitch-angle cosine from μ to $-\mu$ over a very short distance, and a coherent pulse of SEPs can be reflected intact, whereas the loop has focusing that gradually increases as particles move toward the Sun. In the absence of scattering, particles reflect after penetrating to a μ-dependent mirror point. We varied z_{obs}, the distance along the field from the injection footpoint to the observer, and the fits strongly favor the minimum value of 1.1 AU as for an Archimedean spiral. Best-fit results are shown in Figures 8*e*, 8*f*, 9*e*, and 9*f*. Interestingly, the best fit gave a χ^2 value 70% larger than that for the bottleneck with RC = 0.99. The key problem is that the fits give a strong, negative weighted anisotropy at the hump onset, which is not observed.

Thus those three scenarios fail to provide a good fit to the data for reasonable parameters. A better fit is obtained for a bottleneck with RC = 0.99, the physically unreasonable case of a nearly perfect magnetic mirror in interplanetary space. However, one scenario that is equivalent to 100% magnetic mirroring is to inject particles simultaneously along both legs of a magnetic loop. If the loop and injection are symmetric around $z = l/2$, then a particle passing the midpoint of the loop with μ is matched by one passing the other way with $-\mu$. Mathematically, the distribution function behaves as if there is perfect mirroring at the halfway point; physically, the spike corresponds to particles injected along the near leg and the hump to particles from the far leg.

Based on our experience for the loop with injection along one leg, we fix z_{obs} to be 1.1 AU. The best-fit transport parameters are $\lambda_{\parallel} = 2.5$ AU and $l = 4.0$ AU. Although the scenario of injection along both legs of a loop is conceptually similar to a bottleneck beyond Earth with 100% reflection, and the fit value for $l/2$ is similar to that for r_b, there are differences in the details (e.g., $1/L = 0$ at $z = l/2$ for a loop, but not at r_b for a bottleneck), and the best-fit loop model has a χ^2 that is 3 times lower. In Figures 8*g* and 8*h* the thin lines indicate simulated profiles for each injection, which are added to form the Green's function for fitting (*thick lines*). This model has a strong hump and also a slightly negative weighted anisotropy at hump onset, which is then offset

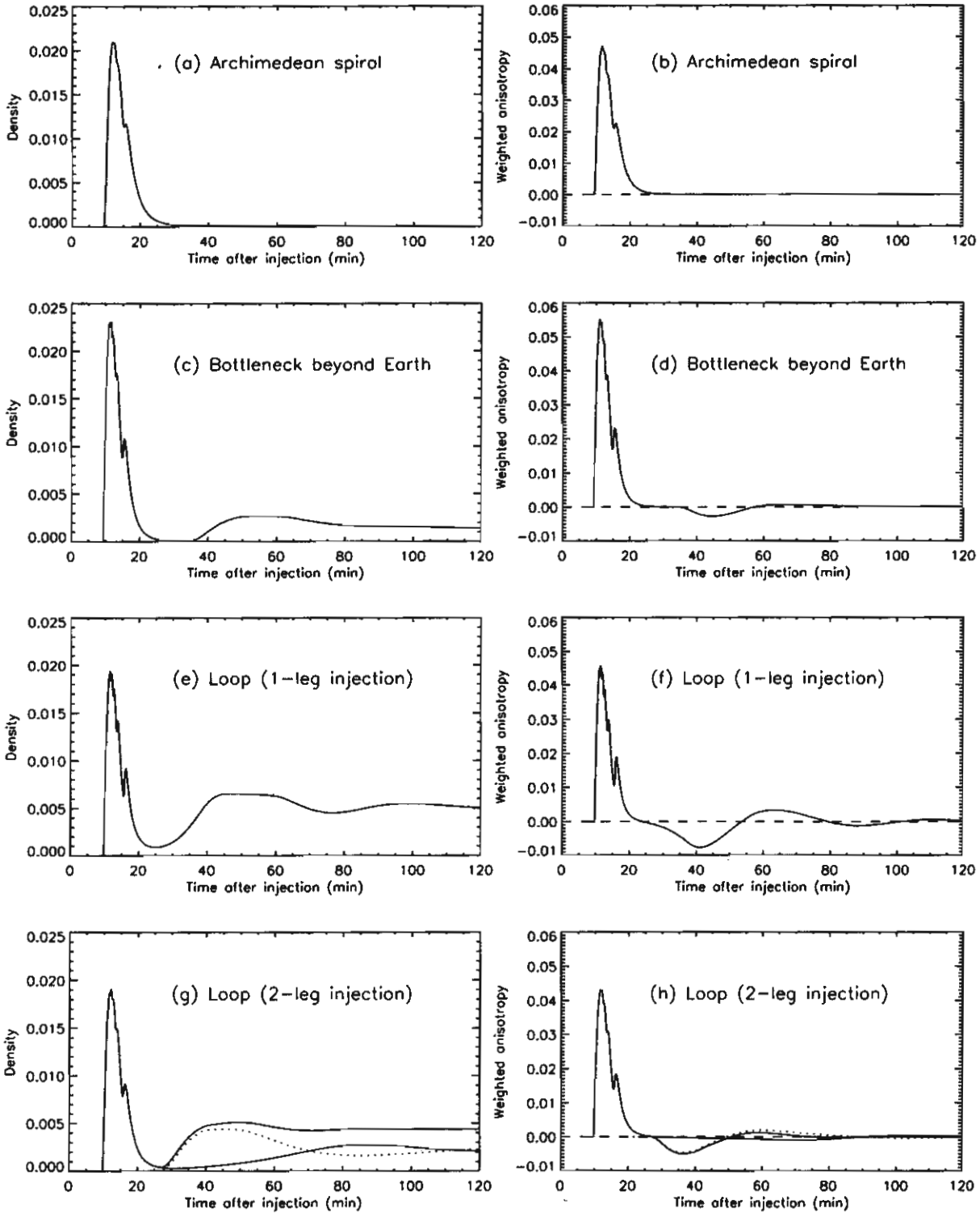

FIG. 8.—Simulations of density (*left panels*) and weighted anisotropy (*right panels*) in arbitrary units as a function of time after an instantaneous injection at the Sun, for (*a–b*) a spiral magnetic field, (*c–d*) a magnetic bottleneck beyond Earth, (*e–f*) injection along the near leg of a closed interplanetary magnetic loop, and (*g–h*) equal injection along both legs of a closed interplanetary magnetic loop. In (*g–h*), the thin line is for injection along the near leg, the dotted line is for injection along the far leg, and the thick line is their sum.

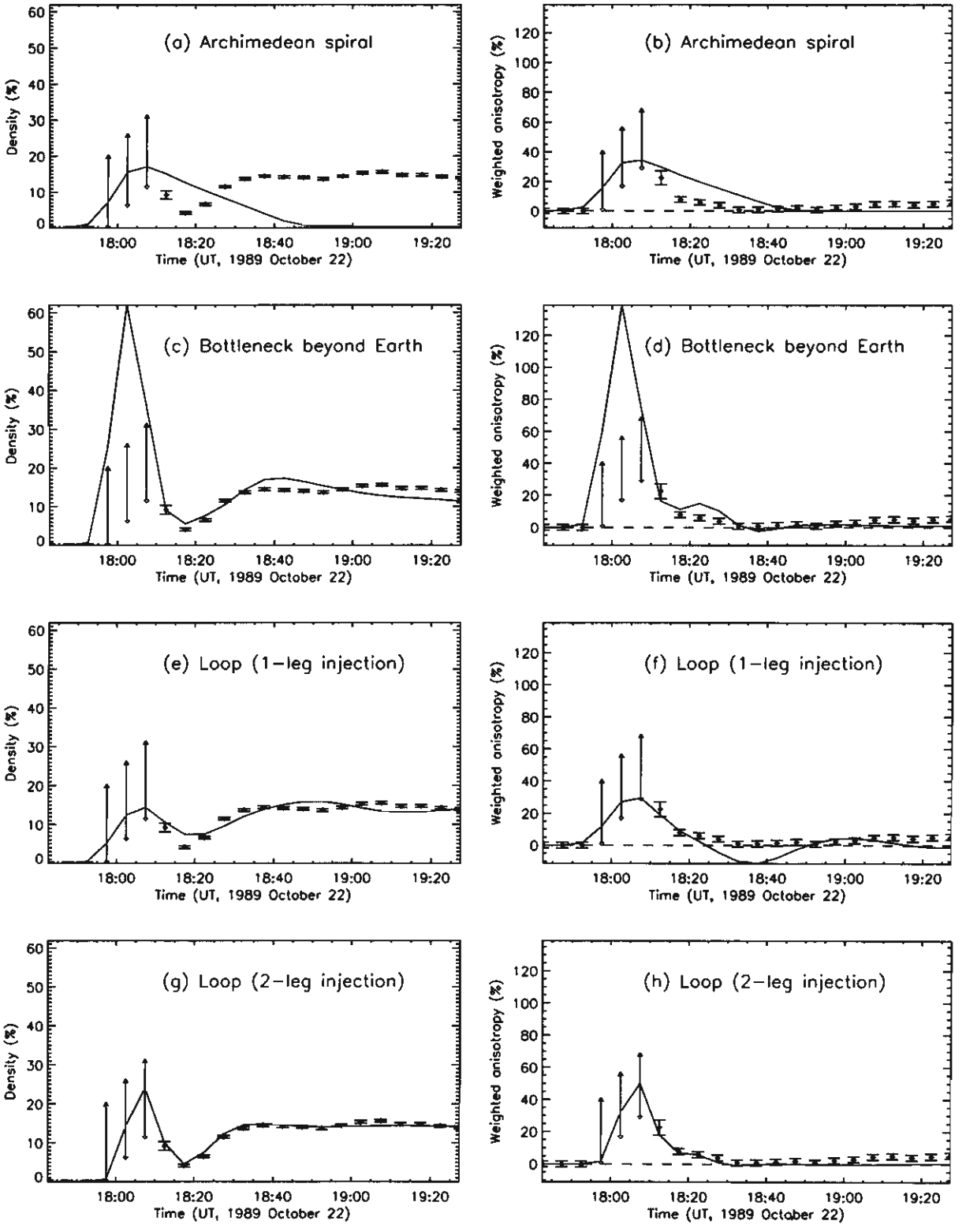

FIG. 9.—Fits to density (*left panels*) and weighted anisotropy (*right panels*) as a function of time for an optimized injection function near the Sun, for (*a*–*b*) a spiral magnetic field, (*c*–*d*) a magnetic bottleneck beyond Earth, (*e*–*f*) injection along the near leg of a closed interplanetary magnetic loop, and (*g*–*h*) equal injection along both legs of a closed interplanetary magnetic loop, the only case that provides a good fit to the data.

TABLE 1

FIT PARAMETERS FOR VARIOUS MAGNETIC FIELD CONFIGURATIONS

CONFIGURATION	χ^2	DEGREES OF FREEDOM	TRANSPORT PARAMETERS[a]					
			λ_r	r_b	RC	$\lambda_\parallel$	l	z_{obs}
Archimedean spiral	19,814.4	32	1.6	...	...			
Bottleneck, RC $\leq$ 0.99	309.9	30	2.0	1.9	0.99			
Bottleneck, RC <0 .95	657.3	30	2.2	1.9	0.95			
Loop, one-leg injection	521.2	31				3.5	2.6	1.1
Loop, two-leg injection	97.4	31				2.5	4.0	...

[a] In units of AU, except RC (reflection coefficient), which is dimensionless.

by continued injection along the near leg to produce bidirectional fluxes of nearly no net weighted anisotropy, as in the data. The optimal fit is visually superior to that for other configurations (see Fig. 9) and matches the five key features of the data.

4.2. *Model Refinements*

Given that the above fits strongly favor a closed interplanetary magnetic loop with injection along both legs, we now ask what further information can be extracted from the data by refining our models to be more physically accurate. On a longer timescale, Figures 1 and 2 indicate that the density eventually does decay with a nearly exponential profile (see also Mathews & Venkatesan 1990). This indicates that an escape mechanism should be included in our transport model, with an escape time T_{esc} fit to the data. Physically, the escape of particles from the loop could result from transport perpendicular to the mean (large-scale) magnetic field. For simplicity, we include a uniform loss rate $1/T_{esc}$, and then we can fit a longer span of the data. (Note that if the late-time data were included in the analysis of the previous section, the least-squares fitting would be dominated by the many data points in the exponential decay, rather than addressing the 5 key features of interest.) A simple exponential fit to the decay yields $T_{esc} = 180$ minutes, a value confirmed in fits to the full data set.

According to our usual procedure, we also examine pitch-angle distributions for the nine polar neutron monitors, which are indeed the raw data from which the density and weighted anisotropy are extracted. To do so, we select one of the four models of the directional distribution. We choose the second-order Legendre polynomial model because it is generally consistent with most other models and should be able to model bidirectional fluxes. Again, the aim is not necessarily to completely model the directional distribution, but rather to extract parameters appropriate for fitting.

Pitch-angle distributions at selected times are shown in Figure 10. (Note that meaningful distributions are not obtained during the spike, for which only two monitors registered an enhancement.) The peak near pitch-angle cosine $\mu = 1$ persists up to 19:35 UT, clearly indicating fresh injection up to 19:25 at the Sun (see also Cramp et al. 1997). At 19:35 UT the observed pitch-angle distribution abruptly changes to be nearly isotropic, possibly with loss-cone features (dips) near $\mu = -1$ and 1 (see Fig. 10*f*). Apparently the injection was cut off sharply at $\approx$19:25, a feature that we now incorporate in the fitting program. Simultaneously, the density and curvature determined by the second-order Legendre model abruptly declines and then the density enters its exponential decay phase (Fig. 11).

The pitch-angle distributions can also indicate the proper value of q, which appears in the parameterization of the pitch-angle scattering coefficient $\varphi(\mu) = A|\mu|^{q-1}(1 - \mu^2)$, a formula from standard quasilinear theory where q is the spectral index of turbulence (see § 3.1). Previous work has found that the clearest indication of q is in data during the late phase of injection, where the directional distribution is in a near steady state. In general, pitch-angle diffusion tends to make $\varphi\partial F/\partial\mu$ a smooth function of μ, so where φ is large the gradient is small, and vice versa. Thus $q = 1.5$, for which φ is small and $\partial F/\partial\mu$ is large for μ near zero can model the step in the intensity j near $\mu = 0$ for the GLE on 2000 July 14 (Bieber et al. 2002), while $q = 1$ gives a smooth variation through $\mu = 0$ for 2001 April 15 (Bieber et al. 2004a). In Figure 10 the profiles for 19:20 UT (panel *d*) and 19:25 UT (panel *e*) show a nearly flat distribution through $\mu = 0$, with freshly injected particles highly collimated near $\mu = 1$, which could indicate a value of $q < 1$. To our knowledge, a value of $q < 1$ has never been previously inferred from time variations of SEP distributions.

To determine appropriate values of q, in addition to fitting the density and weighted anisotropy, we can simultaneously fit the curvature in the pitch-angle distribution. (Recall from § 2.3 that these three quantities are the three coefficients in a second-order Legendre polynomial fit.) For example, at the start of the hump, over $\approx$18:30–19:00 UT, the density and near-zero weighted anisotropy are consistent with a flat (isotropic) distribution, whereas in reality there were bidirectional flows, as shown in Figures 4*a*–4*c*. By including the curvature, we demand that a good fit should reproduce the bidirectional flows. The fit then better addresses the shape of the pitch-angle distribution and is appropriate for examining the effect of q.

For each value of q, simultaneous fits to the density, weighted anisotropy, and curvature as a function of time yield the optimal injection function and transport parameters $\lambda_\parallel$ and l. Results for $q = -1$, 0, and 1 are shown in Table 2 and Figure 11. It is seen that $q = 1$ provides a noticeably worse fit, especially to the curvature throughout the hump and weighted anisotropy at hump onset. The key problem in fits with $q = 1$ or higher is that the density due to the far-leg injection does not rise quickly enough to match the observed sunward intensity, and the optimal fit must include a second injection peak along the near-leg to match the density at hump onset. This second peak is an artifact of the fit, and it results in incorrect values of the weighted anisotropy and curvature. For lower values of q the fits in Figure 11 are improved, although there is still a residual second peak in the injection function for $q = -1$ (Fig. 11, *top panel*). Because the fits still have some residual systematic errors, we do not consider that the quantitative differences in χ^2 indicate an optimal value of q. We are not sure how well our procedure determines the weighted anisotropy and curvature of SEPs at late times, where the anisotropy is weak and there are fluctuations in the directional distribution, as well as possible time variations in the GCR background as the Earth rotates. While the data were fit as shown in Figure 11, we do not take the systematic variations in

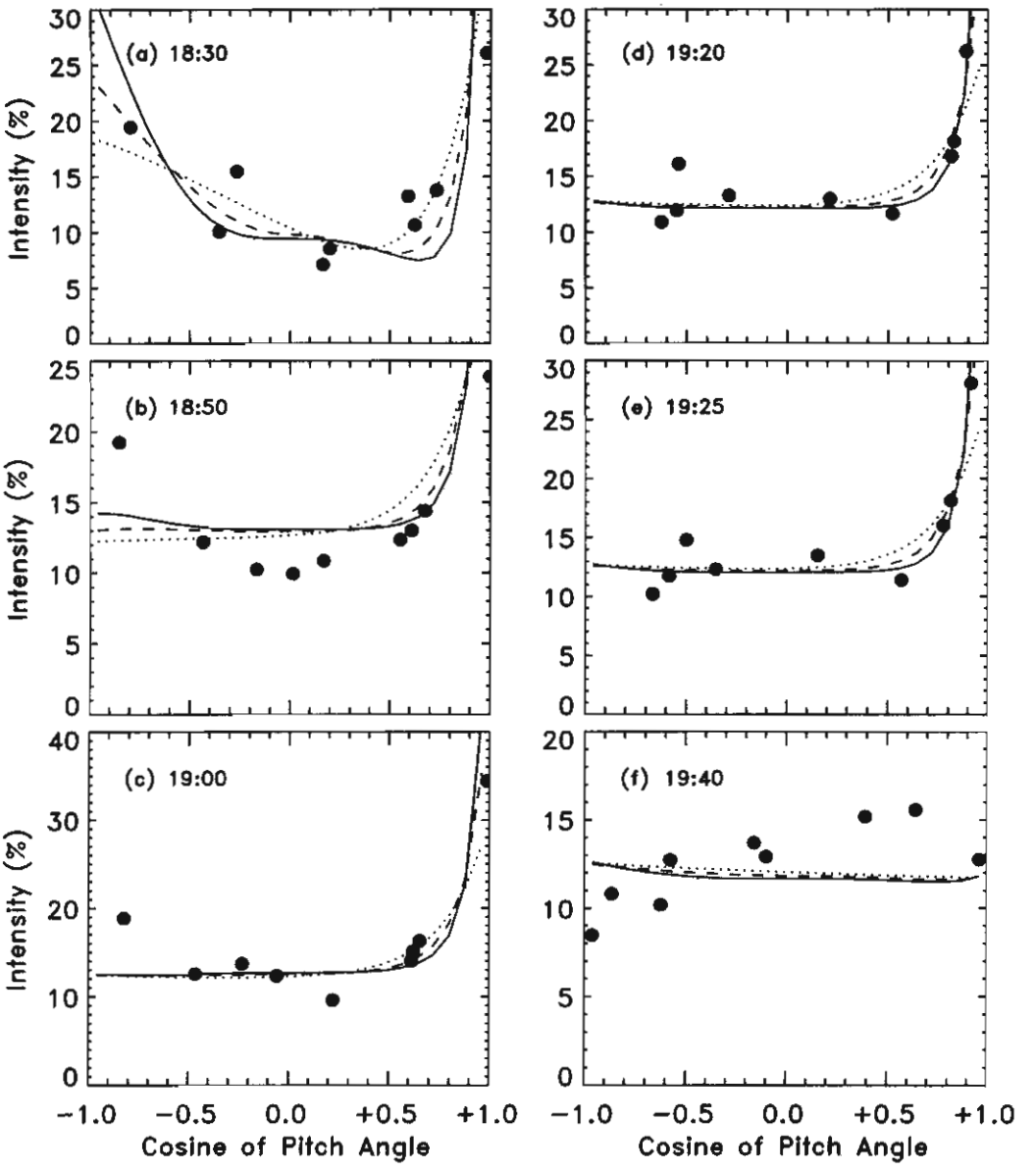

FIG. 10.—Pitch-angle distributions constructed from the observed intensity at each polar neutron monitor station (*solid circles*) as a function of the cosine of its pitch angle relative to the inferred axis of symmetry (Fig. 6), along with model distributions for relativistic proton injection along both legs of a closed interplanetary magnetic loop for $q = -1$ (*solid lines*), $q = 0$ (*dashed lines*), and $q = 1$ (*dotted lines*).

weighted anisotropy and curvature after 19:35 UT to be physically meaningful.

In sum, the least-squares fitting indicates that $q = 1$ provides a substantially worse fit but is unable to provide a clearly optimal value of q.

As a further check, Figure 10 shows how well each fit reproduces the pitch-angle distribution at various times. As a caveat the assignment of a pitch angle to an individual neutron monitor station depends on the estimated axis of symmetry and represents what is actually a distribution of asymptotic directions (see Fig. 3). Furthermore, up to 19:00 UT the axis of symmetry tends to align with the station with highest intensity (McMurdo, MC), an artifact of our procedure. Therefore, we believe that point should not be exactly at $\mu = 1$ and are not concerned when fits yield a maximum intensity at $\mu = 1$ higher than MC. However, a model with a maximum intensity lower than MC is in conflict with the data. In Figure 10 we see that at 18:30 UT, all fits yield bidirectional anisotropy, although $q = -1$ has trouble matching the pitch-angle distribution. At 18:50 UT and 19:00 UT none of the fits correctly treats the sunward flux (at $\mu < 0$).

One important assumption is that the injection along both legs of the loop is taken to be the same. Indeed, we can only weakly constrain the ratio of injection along the far leg to that along the near leg, because the spike was so highly collimated that it was only observed at two stations and we can only derive lower limits to the particle density at that time. Another important model assumption is that $\lambda_{\|}$ is constant along the loop, which is a simplification given that the central part of the loop probably comprises CME ejecta with quite different plasma properties. Given these model assumptions, we do not feel that the detailed quantitative

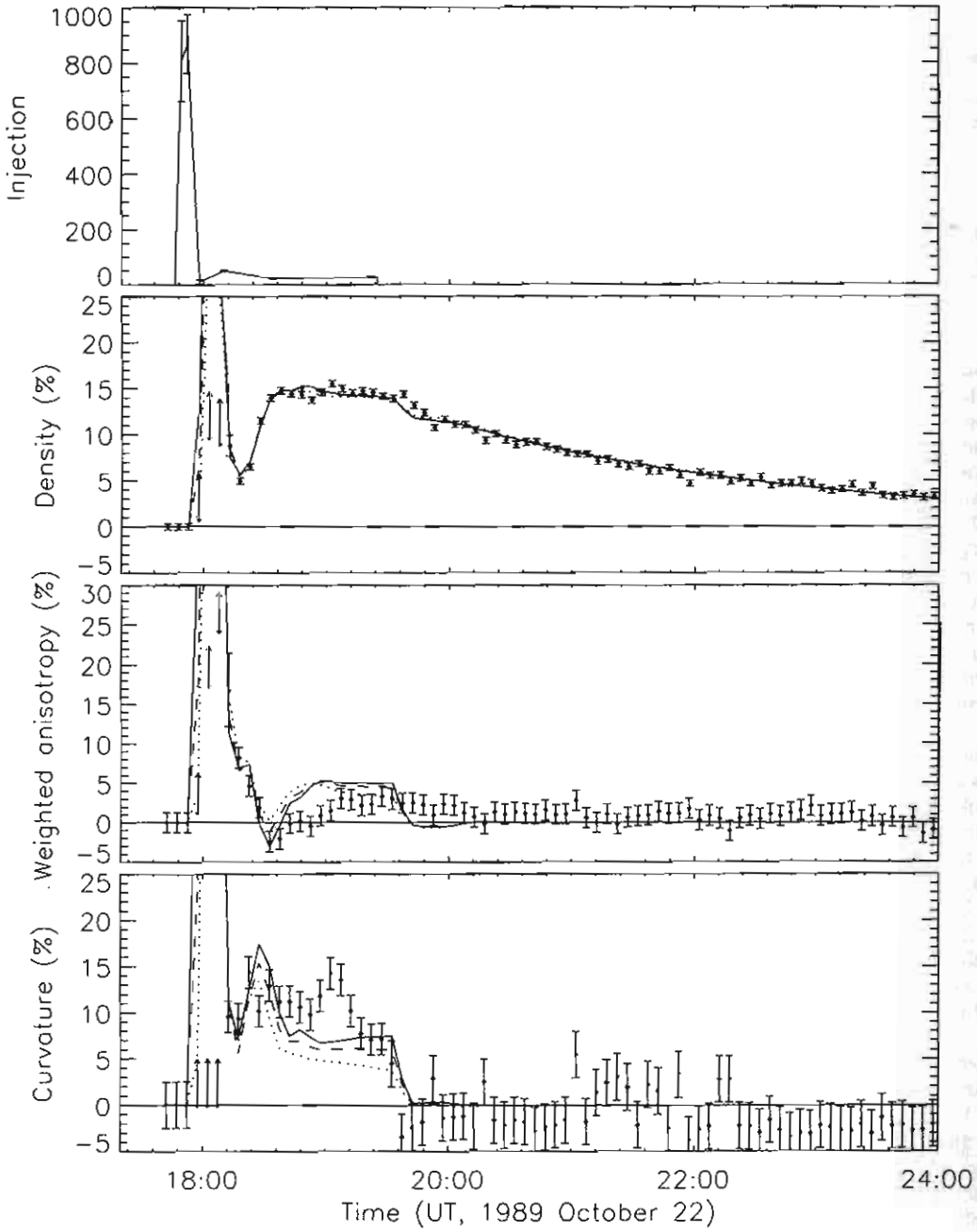

FIG. 11.—Optimal injection profile (arbitrary units) of relativistic solar protons along both legs of a closed interplanetary magnetic loop for $q = -1$, and optimal fits to density, weighted anisotropy, and curvature as a function of time for $q = -1$ (*solid lines*), $q = 0$ (*dashed lines*), and $q = 1$ (*dotted lines*).

TABLE 2

REFINED FIT PARAMETERS FOR INJECTION ALONG BOTH LEGS OF A CLOSED LOOP FOR VARIOUS q-VALUES

q	χ^2	Degree of Freedom	$\lambda_\parallel$ (AU)	l (AU)
1.0	505.7	210	2.0	4.4
0.0	446.9	209	1.4	4.7
−1.0	437.0	209	1.2	4.9

fitting at hump onset is sufficient grounds to rule out high q-values. Indeed, these assumptions are probably responsible for the failure to match the sunward flow in Figures 10*b* and 10*c*.

A more robust feature is the strong enhancement near $\mu = 1$ during the quasi–steady state over 19:15–19:30 UT (see Figs. 10*d*–10*e*), due to continued injection along the near leg superimposed on an isotropized distribution. Since the $q = 1$ model poorly matches the shape of the pitch-angle distribution in this time period, as well as yielding an inferior fit to the time profiles (Fig. 11 and Table 2), we again conclude that $q < 1$.

For q-values from −1 to 0.75 (even lower values of q are not ruled out by the data but are in our opinion physically unlikely)

the optimal scattering mean free path $\lambda_{\parallel}$ is 1.2–2.0 AU, the loop length $l = 4.7 \pm 0.3$ AU, and the injection has a start time (at the Sun) of 17:46 UT, peak time of 17:51 UT, and FWHM of 6 minutes, all with estimated uncertainties of 2 minutes.

5. DISCUSSION

5.1. *Overview*

A key lesson of the present work is the value of precision modeling of the interplanetary transport of solar energetic particles (SEPs). From numerical simulations and careful comparisons with observed time profiles, various reasonable ideas can be excluded. Only after three magnetic field configurations were tested and found to not properly fit the data did we turn to the explanation of injection along both legs of a closed interplanetary magnetic loop, which provides a much better fit. If the analysis of observed time profiles had remained qualitative, the improved explanation would not have surfaced.

The start time of injection of relativistic solar particles, 17:46 UT ±2 minutes, would correspond to Earth observation of electromagnetic emission at 17:54 UT ±2 minutes. This corresponds closely to the actual peak of Hα detection (17:56 UT) and X-rays (17:57 UT). A similar correspondence with the X-ray peak was found to within a few minutes for the GLEs of 2000 July 14 (Bieber et al. 2002), 2003 October 28 (Bieber et al. 2005), and to one-minute accuracy, 2001 April 15 (Bieber et al. 2004a). This indicates a delay between the energetic (rising) phase of the flare and the injection of relativistic particles, which could be attributed to acceleration at a CME shock that takes some time to form.

We concur with Cramp et al. (1997) that there was an extended solar injection. There was an apparent sharp cutoff of injection at 19:30 UT. This cutoff feature, identified in the context of relativistic solar protons, is seen much more dramatically in 24–210 MeV protons (Nemzek et al. 1994). For the relativistic protons, the intensity is continuous at most pitch angles, and the sudden change is only in the outgoing direction, as if the source turned off (Fig. 10). On the other hand, the axis of symmetry changed suddenly at that time to a new direction and then remained roughly constant for the remainder of October 22 (not including time periods of very low anisotropy when the inferred axis can fluctuate widely), implying that the apparent cutoff of injection actually indicates the arrival of a new flux tube with different magnetic connection. This change in magnetic connection is much more evident for the 24–210 MeV protons, causing a nondispersive 30%–50% drop in proton density.

These observations can be understood in terms of magnetic connection to the acceleration region at a traveling interplanetary shock. Relativistic particles were mostly injected at the event onset, when the shock was at low solar altitude, followed by extended injection at a lower intensity (Fig. 11). Before 19:30 UT, the Earth was apparently magnetically connected to the source ever since the start of the GLE. For convenience let us refer to this as the "first flux tube." The second "flux tube," after 19:30, was apparently sufficiently well connected to the source at event onset to obtain almost the same relativistic particle density as the first flux tube, and both flux tubes are apparently loops. The difference is only that the second flux tube magnetically disconnected from the shock at some stage before passing by the Earth at 19:30, so the only observed change at 19:30 was the disappearance of the small outgoing flux. (From a modeling point of view, this is functionally equivalent to a cutoff of injection.) The same scenario can explain the 24–210 MeV proton observations because particles at lower energies typically have a much longer duration of injection by a CME-driven shock. When the second flux tube disconnected from the shock some time after event onset, it therefore received a significantly lower total injection than the first flux tube.

As noted earlier, the polar neutron monitor data cannot precisely determine the ratio of far-leg to near-leg injection because the spike was only caught by two monitors and only lower limits in density are available. While all fitting results assumed a ratio of 1.0 with identical and simultaneous injection functions along the two legs of the loop, we found that multiplying the far-leg injection by anywhere from 0.5 to 3 also yielded reasonable fits. Note that we do not know whether the two legs were physically close together near the Sun, e.g., connected to the same active region. If they were in close proximity, that would provide a natural explanation of why the data are consistent with the same injection function along both legs of the closed interplanetary magnetic loop.

If the relativistic solar protons were accelerated by the CME-driven shock simultaneously along both legs of the loop, those acceleration processes were independent and not synergistic, for the following reasons. The bulk acceleration took place over a FWHM duration of only 6 ± 2 minutes, so particles from one leg could not have traveled $l = 4.7 \pm 0.3$ AU to reach the other in time to serve as seed particles for bulk reacceleration. The inferred values of the mean free path $\lambda_{\parallel}$ are smaller than the loop length l (see Table 2), so the particles from one leg would not survive as a beam to reach the other, and indeed most would suffer magnetic mirroring and would not reach the acceleration region near the Sun.

Our analysis of the 1989 October 22 GLE relies almost exclusively on observations of relativistic solar protons. In the future, a much wider range of corroborating data should be available. For example, the *STEREO* (*Solar Terrestrial Relations Observatory*) mission will provide detailed data on the magnetic field topology. In that case we can apply our precision modeling to probe the conditions of parallel and perpendicular transport of SEPs, providing further information about magnetic loops and the interior of CMEs in interplanetary space. Improved understanding of transport conditions is relevant to understanding certain space weather effects. For example, relativistic solar particles are a space weather hazard to air crews flying polar routes as well as a possible hazard to astronauts on missions to the Moon or Mars. Our observations that these particles can form intense and extremely collimated beams along an axis far from the magnetic field direction, and can come along both legs of an interplanetary magnetic loop, are relevant to shielding requirements for astronaut safety and protection of spaceborne electronic components. In particular, an intense beam of particles can actually arrive in an unpredictable direction (see also Bieber et al. 2005), so it is not sufficient to simply shield against or prepare for such a beam coming from the typical 45° angle of the Archimedean spiral field as one might imagine.

5.2. *Magnetic Fluctuations*

To our knowledge, this is the first report of an inference of $q < 1$ to fit time variations in SEPs. The parameter q enters the transport equation as a parameter in the pitch-angle scattering coefficient $\varphi(\mu) = A|\mu|^{q-1}(1 - \mu^2)$, and in the context of quasilinear theory is identified as the power-law index of the magnetic turbulence power spectrum (Jokipii 1971) at wavenumbers k resonant with the particle rigidity of interest. More specifically, Matthaeus et al. (1990) showed that interplanetary fluctuations are predominantly at wave vectors nearly parallel to the mean field (the "slab" component) and nearly perpendicular to the mean field (the "two-dimensional" component, and particles undergo

resonant scattering with the slab component (Bieber et al. 1994). The power spectrum has long been known to comprise a Kolmogorov spectrum, i.e., with power-law index $q \sim 5/3$, over an inertial range, and a rollover at low k to a roughly constant spectrum (Jokipii & Coleman 1968), i.e., $q \sim 0$. The rollover wavenumber k_c corresponds to the turbulent correlation length $l_c \sim 1/k_c$. Therefore, it is not unreasonable that very high-energy particles would experience $q < 1$.

What is unusual is to observe $q < 1$ for 1–3 GV protons. Based on a compilation by Bieber et al. (1994), Leerungnavarat et al. (2003) point out (and illustrate in their Fig. 2) that the spectral rollover, with $q \sim 1$, typically corresponds to a proton rigidity of ~10 GV. Therefore, under normal solar wind conditions one would expect 1–3 GV protons to resonate with turbulent fluctuations in or close to the inertial range. Indeed, previous analyses for this energy range were consistent with $q = 1.5$ on 2000 July 14 (Bieber et al. 2002) and $q = 1.0$ on 2001 April 15 (Bieber et al. 2004a).

We therefore postulate that the unusually low value of q inferred in this work for 1989 October 22 was associated with the closed interplanetary magnetic loop configuration. We infer that the correlation length of slab fluctuations was at least an order of magnitude smaller than usual, i.e., $\lesssim$0.002 AU instead of ~0.02 AU. This makes k_c unusually high and yields $q < 1$ in the wavenumber region resonant with 1–3 GV protons.

There is an observational precedent for unusual magnetic fluctuations in closed loops. Previous work has found that a magnetic cloud (comprising closed loops) embedded in CME plasma can have unusually weak fluctuations (Burlaga et al. 1981) and a particularly weak slab component (Leamon et al. 1998). As the slab component is responsible for resonant scattering of particles (Bieber et al. 1994), the results of Leamon et al. (1998) are also consistent with the long mean free path of $\lambda_{\parallel} = 1.2$–$2.0$ AU inferred in the present work. Note that Torsti et al. (2004) found a very long mean free path inside the magnetic cloud of 1998 May 2–3, and the much earlier work of Tranquille et al. (1987) identified weak particle scattering and low magnetic fluctuations at a time of intense magnetic fields.

We note that the results of Leamon et al. (1998) for a magnetic cloud are similar to those of Buttighoffer (1998), Buttighoffer et al. (1999), and Smith et al. (2001, 2004) for rarefaction regions of open magnetic field lines in the solar wind. Very weak particle scattering was also observed in such regions by Buttighoffer (1998). Mullan et al. (2003) proposed the interesting physical explanation that MHD waves are refracted away from regions of high Alfvén speed. That work aimed to explain the low fluctuations and very low slab fluctuations observed by Smith et al. (2001) for rarefaction regions, but it could clearly apply to magnetic clouds in CMEs as well. Indeed, if one imagines a cylindrical region where the Alfvén speed is high, external fluctuations with wave vector aligned nearly along the mean field (i.e., slab fluctuations) can undergo total reflection and fail to penetrate the cylinder, while other, oblique waves are more likely to enter. Work by Reames et al. (2001) and Crooker et al. (2003) indeed found a correlation between strong particle anisotropy, i.e., weak scattering, and the plasma β parameter, which in the context of Mullan et al. (2003) can be interpreted as a proxy for the Alfvén speed.

Therefore, the long mean free path inferred in the present work is part of a coherent picture that emerges from a large body of work in the literature: regions of high Alfvén speed refract away magnetic fluctuations, especially the slab fluctuations responsible for particle scattering, and provide "highways" (Torsti et al. 2004) of particle transport with low scattering and strong anisotropy. To this picture we add the inference of $q < 1$ and an unusually small correlation length $l_c \lesssim 0.002$ AU inside a closed loop, for which we cannot at present provide a physical explanation.

5.3. *Interpreting the Decay Rate*

The decay in density at late times is quite slow by the standards of GLE observations and favors a loop configuration in which the particles can be trapped for extended times. Our implementation of the loop geometry in the transport code traps particles very effectively, so to explain the data we introduce an escape process with an exponential decay time of 3 hr. Now we address the physical mechanism of this escape and the interpretation of the timescale.

First note that there is very little escape due to parallel transport. While particles could in principle be absorbed at the solar surface, the focusing (magnetic mirroring) there is very intense, and very few particles reach such low altitudes. Indeed the transport simulation code includes absorbing boundaries at 0.01 AU (≈2 solar radii) from the solar center, and there is no significant loss in the particle phase-space density, which quickly becomes constant in time, space, and direction. This leaves three reasonable possibilities: (1) adiabatic deceleration, which removes particles from the detected energy range; (2) perpendicular drifts; and (3) perpendicular diffusion. These mechanisms could take place in the central part of the loop, presumably a magnetic cloud embedded in CME plasma, and/or in the legs with plasma and magnetic field conditions that are more typical of the solar wind.

Adiabatic deceleration was actually not included in our treatment of the loop configuration for reasons described in § 3.1, so this is a candidate process to explain the density decay. The rate of density decay due to adiabatic deceleration is $(2/3)(\delta - 1)v_{sw}/r$ for a radial solar wind of constant speed (Ruffolo 1995), where δ is the spectral index, taken to be 6.5 for the time period of interest (Fig. 5), and we use a solar wind speed $v_{sw} = 600$ km s^{-1}. At Earth this yields a decay timescale of 18.9 hr, much longer than the observed value of 3 hr. Given that observed major CMEs are typically ~60° in extent, and based on the inferred loop length of 4.7 AU, we estimate that the volume-averaged rate of decay over the loop yields a value similar to that at Earth. Thus adiabatic deceleration does not explain the density decay, and we can justify its neglect in the transport simulations in loops at these relativistic energies.

This implies that perpendicular transport processes are needed, and the observed 3 hr decay time heralds a new type of information on the perpendicular transport of energetic particles in space. Such transport processes include systematic drifts and random diffusion.

Particles orbiting Archimedean magnetic field lines in the solar equatorial plane experience curvature and gradient drifts in the same direction, either southward or northward depending on the magnetic field direction and particle sign. (Note that the theorem of Jones et al. [1998], if applicable, would imply that particles remain confined to a nearly constant heliolatitude; however, there are drifts along or counter to the interplanetary electric field, so their assumption of energy conservation does not apply.) However, inside a magnetic cloud, the coiling of magnetic field lines can confine the drift orbits to closed surfaces inside the cloud, as in tokamak fusion plasmas. It is not clear whether the coiling of magnetic field lines persists throughout the flux rope, e.g., in the legs connecting back to the Sun. Drawings by Burlaga et al. (1990) and Vandas et al. (1996) show coiling with a lower pitch in the legs, which is reasonable in the sense that the CME is driven forward with high speed and the legs should be stretched. In the leg regions with lower pitch (or possibly no coiling at all) near the Sun, a lower fraction of the drift orbits would remain confined to the loop.

Therefore, it is likely that many drift orbits are confined in the central, magnetic cloud portion of the loop and not confined in

the legs. Then escape from the loop due to drifts takes place preferentially near the Sun. The escape can be an exponential process because of random pitch-angle scattering into a loss cone where particles can be removed by drifts near the Sun. The pitch-angle distribution in Figure 10*f* seems to exhibit loss cone features consistent with that idea, although our analysis of polar neutron monitor data during the decay phase does not consistently show loss cone features at all times. Note that the issue of how relativistic solar protons escape from a closed magnetic loop is closely related to the issue of second-stage Forbush decreases of GCRs (Cane et al. 1994), where the depth of the decrease is related to how well Galactic particles can get into the loop. The bidirectional flows of GCRs discussed in § 2.2 are consistent with preferential inflow at the portions of the loop near the Sun. Without knowing the precise three-dimensional magnetic topology for a given CME, it is very difficult to estimate the rate at which drifts cause particles to drain out of (or enter into) the loop; for different coiling pitch and stretching of coils in the legs, very different escape rates can result.

Another possibility is that particles escape by means of perpendicular diffusion. For escape from the uniform interior of a tube of circular cross-section, the long-time decay rate of the particles (uniformly distributed over the volume of the tube) is given by

$$\frac{1}{T} = \kappa_\perp \frac{x^2}{R^2}, \tag{10}$$

where $\kappa_\perp$ is the average perpendicular diffusion coefficient, $x = 2.4$ is the first zero of the Bessel function J_0, and R is the average radius of the tube (averages are over the length of the tube). (See also Wibberenz et al. 1998.) Here we measure $T = 3$ hr, so $\kappa_\perp = (1.6 \times 10^{-5}\ \mathrm{s}^{-1})R^2$. For example, if $R = 0.2$ AU, the inferred diffusion coefficient would be $\kappa_\perp = 1.4 \times 10^{20}\ \mathrm{cm}^2\ \mathrm{s}^{-1}$, which corresponds to a perpendicular mean free path $\lambda_\perp \equiv 3\kappa_\perp / v \approx 0.001$ AU, where v is the particle speed. This value is in excellent agreement with the recently proposed "nonlinear guiding center" (NLGC) theory of perpendicular diffusion (Matthaeus et al. 2003; Bieber et al. 2004b). According to an approximate expression given by equation (56) of Shalchi et al. (2004),

$$\lambda_\perp \approx 0.067(\delta B^2 / B_0^2)^{2/3} l_c^{2/3} \lambda_\parallel^{1/3}, \tag{11}$$

where we have taken $\nu = 5/6$ in the notation of Shalchi et al. According to Zank et al. (2004, see their Fig. 5), $\lambda_\perp$ displays surprisingly little radial variation, at least beyond 1 AU. In the absence of better information, we assume that $\lambda_\perp$ is also constant in the inner heliosphere and adopt values characteristic of 1 AU for the parameters in equation (9). We therefore take $\delta B^2 = B_0^2$ (see, e.g., Bieber et al. 1994), $l_c = 0.002$ AU (see § 5.2), and $\lambda_\parallel = 1.6$ AU. We obtain $\lambda_\perp = 0.0012$ AU, which is precisely the value required to explain the 3 hr decay time.

There have been reports of open field line regions embedded inside magnetic clouds in association with an inflow of GCRs (Bothmer et al. 1997; Cane et al. 2001). Given the smooth decay profile, Earth itself probably did not encounter such a region during the decay phase of the 1989 October 22 GLE, but a nearby region of open field lines could provide a rapid escape path, and equation (10) would underestimate the decay rate. The presence or absence of such an escape path inside the magnetic cloud could lead to strong event-to-event variability.

In sum, we interpret the 3 hr decay timescale of the 1989 October 22 GLE as the time constant for particles to escape from the loop. Two possible mechanisms, perpendicular drifts or diffusion, can explain this timescale. In the drift mechanism, escape is likely to occur predominantly in portions of the loop near the Sun.

6. CONCLUSIONS

The following are the conclusions of our analysis of data from nine polar neutron monitors for the unusual ground-level enhancement of relativistic solar protons on 1989 October 22:

1. The five key features of the density and anisotropy profiles (see § 4.1) are not well explained by magnetic field configurations of an Archimedean spiral, a bottleneck beyond Earth, or a loop with injection along one leg. They are well explained by injection along both legs of a closed interplanetary magnetic loop that included the Earth.
2. Observed time profiles can be understood in terms of standard transport processes of scattering and focusing, with the additional process of escape from the loop.
3. Relativistic solar protons were injected near the Sun starting at 17:46 UT and peaking at 17:51 UT, with a FWHM duration of 6 minutes (all ±2 minutes). There was also extended injection for ≈90 minutes at a lower level, followed by a cutoff presumably associated with changing magnetic connection to the source.
4. Observed pitch-angle distributions indicate $q < 1$, where q is a transport parameter identified with the spectral index of magnetic fluctuations. To our knowledge such a low value has not previously been inferred from solar particle observations.
5. Relativistic protons escaped from the loop with a time constant of 180 minutes, which is interpreted as an escape time due to transport perpendicular to the large-scale magnetic field.
6. The length of the loop is inferred to be 4.7 ± 0.3 AU, and the parallel mean free path is estimated as 1.2–2.0 AU, depending on the value of q.
7. These results are consistent with an overall picture from various reports in the literature of low magnetic fluctuations, very low slab fluctuations, and long scattering mean free paths in magnetic loops and other regions of high Alfvén speed. The present results suggest that the turbulent correlation length can be unusually short in magnetic loops.

We thank our colleagues at IZMIRAN (Russia), the Polar Geophysical Institute (Russia), and the Australian Antarctic Division for furnishing data. We also thank Pete Riley, Dermott Mullan, and Alejandro Sáiz for useful discussions. Terre Adelie data were kindly provided by the French Polar Institute (IPEV, Brest) and by Paris Observatory. This research was partially supported by the Thailand Research Fund, the Rachadapisek Sompoj Fund of Chulalongkorn University, and the US National Science Foundation (grant ATM-0000315).

REFERENCES

Bai, T. 1987, ApJ, 314, 795
Bame, S. J., Asbridge, J. R., Feldman, W. C., Gosling, J. T., & Zwickl, R. D. 1981, Geophys. Res. Lett., 8, 173
Bavassano, B., Iucci, N., Lepping, R. P., Signorini, C., Smith, E. J., & Villoresi, G. 1994, J. Geophys. Res., 99, 4227
Beeck, J., Mason, G. M., Hamilton, D. C., Wibberenz, G., Kunow, H., Hovestadt, D., & Klecker, B. 1987, ApJ, 322, 1052
Bieber, J. W., et al. 2002, ApJ, 567, 622
Bieber, J. W., Clem, J., Evenson, P., Pyle, R., Ruffolo, D., & Sáiz, A. 2005, Geophys. Res. Lett., 32, L03S02

Bieber, J. W., & Evenson, P. 1987, Proc. 20th Int. Cosmic Ray Conf. (Moscow), 3, 151
———. 1991, Proc. 22nd Int. Cosmic Ray Conf. (Dublin), 3, 129
———. 1995, Proc. 24th Int. Cosmic Ray Conf. (Rome), 4, 1316
Bieber, J. W., Evenson, P., Dröge, W., Pyle, R., Ruffolo, D., Rujiwarodom, M., Tooprakai, P., & Khumlumlert, T. 2004a, ApJ, 601, L103
Bieber, J. W., Evenson, P. A., & Pomerantz, M. A. 1986, J. Geophys. Res., 91, 8713
———. 1990, Eos, 71, 1027
Bieber, J. W., Matthaeus, W. H., Shalchi, A., & Qin, G. 2004b, Geophys. Res. Lett., 31, L10805
Bieber, J. W., Matthaeus, W. H., Smith, C. W., Wanner, W., Kallenrode, M.-B., & Wibberenz, G. 1994, ApJ, 420, 294
Bothmer, V., et al. 1997, Proc. 25th Int. Cosmic Ray Conf. (Durban), 1, 333
Burlaga, L. F., Hundhausen, A. J., & Zhao, X.-P. 1981, J. Geophys. Res., 86, 8893
Burlaga, L. F., Lepping, R., & Jones, J. 1990, in Physics of Flux Ropes, ed. C. T. Russell, E. R. Priest, & L. C. Lee (AGU Geophys. Monogr. 58; Washington, D.C.: AGU), 373
Buttighoffer, A. 1998, A&A, 335, 295
Buttighoffer, A., Lanzerotti, L. J., Thomson, D. J., Maclennan, C. G., & Forsyth, R. J. 1999, A&A, 351, 385
Cane, H. V., & Richardson, I. G. 1995, J. Geophys. Res., 100, 1755
Cane, H. V., Richardson, I. G., von Rosenvinge, T. T., & Wibberenz, G. 1994, J. Geophys. Res., 99, 21429
Cane, H. V., Richardson, I. G., Wibberenz, G., Dvornikov, V. M., & Sdobnov, V. E. 2001, Proc. 27th Int. Cosmic Ray Conf. (Hamburg), 9, 3531
Cliver, E. W., Kahler, S. W., & Reames, D. V. 2004, ApJ, 605, 902
Compton, A. H., & Getting, I. A. 1935, Phys. Rev., 47, 817
Cramp, J. L., Duldig, M. L., Flückiger, E. O., Humble, J. E., Shea, M. A., & Smart, D. F. 1997, J. Geophys. Res., 102, 24237
Crooker, N. U., Larson, D. E., Kahler, S. W., Lamassa, S. M., & Spence, H. E. 2003, Geophys. Res. Lett., 30, 1619
Danilova, O. A., Tyasto, M. I., Vashenyuk, E. V., Gvozdevsky, B. B., Kananen, H., & Tanskanen, P. 1999, Proc. 26th Int. Cosmic Ray Conf. (Salt Lake City), 6, 399
Dröge, W. 2003, ApJ, 589, 1027
Duggal, S. P. 1979, Rev. Geophys. Space Phys., 17, 1021
Duldig, M. L., et al. 1993, Proc. Astron. Soc. Australia, 10, 211
Earl, J. A. 1976, ApJ, 206, 301
Flückiger, E. O., Kobel, E., Smart, D. F., Shea, M. A., Humble, J. E., Cramp, J. L., & Duldig, M. L. 1993, Eos, 74, 487 (Fall Meet. Suppl.)
Hatzky, R., Kallenrode, M.-B., & Schmidt, J. 1997, Proc. 25th Int. Cosmic Ray Conf. (Durban), 1, 245
Jokipii, J. R. 1966, ApJ, 146, 480
———. 1971, Rev. Geophys. Space Phys., 9, 27
Jokipii, J. R., & Coleman, P. J. 1968, J. Geophys. Res., 73, 5495
Jones, F. C., Jokipii, J. R., & Baring, M. G. 1998, ApJ, 509, 238
Kahler, S. W. 1993, J. Geophys. Res., 98, 5607
Kallenrode, M.-B., Wibberenz, G., & Hucke, S. 1992, ApJ, 394, 351
Kocharov, L., Vainio, R., Kovaltsov, G. A., & Torsti, J. 1998, Sol. Phys., 182, 195
Lario, D., Sanahuja, B., & Heras, A. M. 1998, ApJ, 509, 415
Leamon, R. J., Smith, C. W., & Ness, N. F. 1998, Geophys. Res. Lett., 25, 2505
Lee, M. A., & Ryan, J. M. 1986, ApJ, 303, 829
Leerungnavarat, K., Ruffolo, D., & Bieber, J. W. 2003, ApJ, 593, 587
Lin, Z., Bieber, J. W., & Evenson, P. 1995, J. Geophys. Res., 100, 23543
Makhmutov, V. S., Kaufmann, P., Costa, J. E. R., Lagrotta, P. R., Magun, A., Arzner, K., Bazilevskaya, G. A., & Shea, M. A. 2002, Adv. Space Res., 29, 2101
Mason, G. M., Gloeckler, G., & Hovestadt, D. 1984, ApJ, 280, 902
Mathews, T., & Venkatesan, D. 1990, Nature, 345, 600
Matthaeus, W. H., Goldstein, M. L., & Roberts, D. A. 1990, J. Geophys. Res., 95, 20673
Matthaeus, W. H., Qin, G., Bieber, J. W., & Zank, G. 2003, ApJ, 590, L53
Meyer, P., Parker, E. N., & Simpson, J. A. 1956, Phys. Rev., 104, 768
Mullan, D. J., Smith, C. W., Ness, N. F., & Skoug, R. M. 2003, ApJ, 583, 496
Nemzek, R. J., Belian, R. D., Cayton, T. E., & Reeves, G. D. 1994, J. Geophys. Res., 99, 4221
Nutaro, T., Riyavong, S., & Ruffolo, D. 2001, Comput. Phys. Commun., 134, 209
Palmer, I. D. 1982, Rev. Geophys. Space Phys., 20, 335
Palmer, I. D., Allum, F. R., & Singer, S. 1978, J. Geophys. Res., 83, 75
Parker, E. N. 1958, ApJ, 128, 664
Reames, D. V. 1990, ApJ, 358, L63
Reames, D. V., Ng, C. K., & Berdichevsky, D. 2001, ApJ, 550, 1064
Richardson, I. G., & Cane, H. V. 1993, J. Geophys. Res., 98, 15295
———. 1996, J. Geophys. Res., 101, 27521
Richardson, I. G., Dvornikov, V. M., Sdobnov, V. E., & Cane, H. V. 2000, J. Geophys. Res., 105, 12579
Roelof, E. C. 1969, in Lectures in High Energy Astrophysics, ed. H. Ögelmann & J. R. Wayland (NASA SP-199; Washington, DC: NASA), 111
Ruffolo, D. 1991, ApJ, 382, 688
———. 1995, ApJ, 442, 861
———. 1997, ApJ, 481, L119
Ruffolo, D., Khumlumlert, T., & Youngdee, W. 1998, J. Geophys. Res., 103, 20591
Shalchi, A., Bieber, J. W., & Matthaeus, W. H. 2004, ApJ, 604, 675
Shea, M. A. 1990, Proc. 21st Int. Cosmic Ray Conf. (Adelaide), 12, 196
Shea, M. A., & Smart, D. F. 1997, Proc. 25th Int. Cosmic Ray Conf. (Durban), 1, 129
Smith, C. W., Mullan, D. J., & Ness, N. F. 2004, J. Geophys. Res., 109, A01111
Smith, C. W., Mullan, D. J., Ness, N. F., Skoug, R. M., & Steinberg, J. 2001, J. Geophys. Res., 106, 18625
Stoker, P. 1985, Proc. 19th Int. Cosmic Ray Conf. (La Jolla), 4, 114
Torsti, J., Riihonen, E., & Kocharov, L. 2004, ApJ, 600, L83
Tranquille, C., Sanderson, T. R., Marsden, R. G., Wenzel, K.-P., & Smith, E. J. 1987, J. Geophys. Res., 92, 6
Tsyganenko, N. A. 1989, Planet. Space Sci., 37, 5
Vandas, M., Fischer, S., Dryer, M., Smith, Z., & Detman, T. 1996, J. Geophys. Res., 101, 2505
Wibberenz, G., le Roux, J. A., Potgieter, M. S., & Bieber, J. W. 1998, Space Sci. Rev., 83, 309
Wilson, J. W., Goldhagen, P., Rafnsson, V., Clem, J. M., De Angelis, G., & Friedberg, W. 2003, Adv. Space Res., 32, 3
Zank, G. P., Li, G., Florinski, V., Matthaeus, W. H., Webb, G. M., & le Roux, J. A. 2004, J. Geophys. Res., 109, A04107

Random Walk of Magnetic Field Lines in Non-axisymmetric Turbulence

D. Ruffolo[1], P. Chuychai[1,2,3], and W. H. Matthaeus[3]

ABSTRACT

The random walk of turbulent magnetic field lines strongly affects transport of energetic particles in astrophysical plasmas, but is not well understood for general configurations that lack rotational symmetry. Here we derive non-perturbative field line diffusion coefficients for magnetic fluctuations that are non-axisymmetric with respect to the mean magnetic field. We consider a superposition of slab plus two-dimensional fluctuations, a model that has proven useful in heliospheric studies. Two independent parameters are introduced to allow polarization of the slab component and stretching of the two-dimensional component. With the assumptions of homogeneity, the diffusion approximation, and Corrsin's independence hypothesis, we derive two coupled biquadratic equations for the diffusion coefficients. The results and underlying assumptions are confirmed by numerical simulations. Special cases of interest include the counter-intuitive results that enhanced fluctuations in one direction lead to decreased diffusion in other direction, and that extreme non-axisymmetry leads to diffusion coefficients proportional to the root-mean-squared two-dimensional fluctuation.

Subject headings: magnetic fields — turbulence — diffusion

[1]Department of Physics, Faculty of Science, Mahidol University, Bangkok 10400, Thailand.
david_ruffolo@yahoo.com

[2]Department of Physics, Faculty of Science, Chulalongkorn University, Bangkok 10330, Thailand.
paeng@bartol.udel.edu

[3]Bartol Research Institute, University of Delaware, Newark, DE 19716.
yswhm@bartol.udel.edu

1. Introduction

Turbulent motions, nearly universal in tenuous astrophysical plasmas, lead to magnetic turbulence and the random walk of magnetic field lines. The field lines define the magnetic topology and play an important physical role by guiding the motion of charged particles. The classic work of Jokipii (1966) and Jokipii & Parker (1968) expressed a relationship between the random walk of field lines in magnetic turbulence and the diffusion of energetic charged particles perpendicular to the mean magnetic field in astrophysical plasmas, for the case of weak fluctuations, often described as the quasilinear (QLT) limit.

Recent work on the field line random walk has stressed the importance of large amplitude fluctuations, as well as the generally anisotropic character of MHD turbulence (Isichenko 1991a,b; Wang et al. 1995; Matthaeus et al. 1995; Pommois et al. 1999). This involves not only extending the analytical methods beyond the QLT approach, but also appropriately representing more complex three dimensional magnetic turbulence properties. In particular, a two-component "2D+slab" model adds slab and two-dimensional turbulence to provide a useful model of solar wind fluctuations (Matthaeus et al. 1990; Bieber et al. 1996). This model of anisotropic turbulence is sufficiently simple to allow analytic calculations of ensemble average properties while still including a rich variety of local topological effects (Ruffolo et al. 2003; Chuychai et al. 2005). The anisotropy is strong in the low latitude solar wind, with a roughly 80:20 ratio of 2D to slab turbulent energy (Bieber et al. 1994, 1996), and is even stronger in magnetic clouds (Leamon et al. 1998) and rarefaction regions in the solar wind (Smith et al. 2001, 2004). Recent results suggest that the fast wind has lower 2D admixture, with perhaps a 50:50 ratio of energies (Dasso et al. 2005). The anisotropic nature of solar wind turbulence has been shown to have interesting physical effects. Bieber et al. (1994) showed that this anisotropy may resolve the long-standing discrepancy between theoretical and observed mean free paths of solar energetic particles. Matthaeus et al. (1995) derived analytic formulae for the field line random walk in two-component turbulence, later confirmed by computer simulations (Gray et al. 1996), that indicate diffusion tending as b^2/B_0^2 for slab turbulence (Jokipii & Parker 1968) but as b/B_0 for the two-dimensional component. Note, however, that many of the classic concepts of transport phenomena in turbulent media are based on implicit assumptions of nearly isotropic turbulence. Ruffolo et al. (2004) showed that in two-component turbulence, the separation of magnetic field lines only develops an exponential form (Rechester & Rosenbluth 1978) when the slab component dominates the field line random walk, and the Kubo number that classically defines quasilinear vs. percolative behavior (e.g., Isichenko 1991a,b) needs to be modified for strongly anisotropic turbulence.

Understanding has greatly improved by considering the anisotropy of magnetic turbulence; however, most of this work has continued to assume *axisymmetry*, with some notable

exceptions (e.g., Pommois et al. 1999, 2001). Axisymmetry about the z-axis (usually the coordinate along the mean field) implies that statistical properties of the turbulent field are rotationally symmetric in the perpendicular coordinates x and y. However, there are indications that the variances of magnetic fluctuations may be non-axisymmetric in some cases of interest. The classic work of Belcher & Davis (1971) indicated a roughly 4 : 3 ratio in solar wind fluctuation energy in the $\hat{z} \times \hat{r}$ direction relative to the orthogonal direction (Table 6 of that work) along the *Mariner 5* Venus flyby trajectory. Recent studies also suggest a possible role of non-axisymmetric fluctuations in enhanced latitudinal transport of cosmic rays at high heliographic latitudes (Jokipii et al. 1995; Burger & Hattingh 1998). Note that the Archimedean spiral magnetic field (Parker 1958) in the outer heliosphere is mainly in the azimuthal direction, so the two perpendicular coordinates are r and θ. However, the solar wind flow is essentially radial with a small deceleration, so the solar wind plasma is greatly stretched in θ with a slight compression in r. This difference in the two directions perpendicular to the mean magnetic field may well induce a degree of non-axisymmetry in magnetic turbulence in the outer heliosphere (Jokipii 1973), even if there is some transfer of energy between these two perpendicular directions due to dynamical couplings. For these reasons there is ample motivation to extend our understanding of axisymmetric turbulence to the more general case of non-axisymmetry.

In this work we develop a theory for the non-axisymmetric field line random walk in a general nonperturbative scheme (Matthaeus et al. 1995). This approach is useful for transverse fluctuations in general, and is explicitly applied here to non-axisymmetric two-component turbulence. The non-axisymmetry includes both polarization of the slab component and stretching of the two-dimensional component in wavenumber space. Our principal result is a set of coupled biquadratic equations in the diffusion coefficients D_x and D_y. Computer simulations are also performed, which verify the analytic solutions and justify the underlying assumptions. An interesting finding is that increased fluctuations in one direction can inhibit the field line random walk in the other direction. It is also found that the limit of extreme non-axisymmetry leads to a first-order dependence of the field line random walk on b/B_0. We derive closed-form solutions for several limiting cases, which should find immediate application in heliospheric scattering problems such as cosmic ray modulation.

2. Analytic theory

The present work considers statistically homogeneous, non-axisymmetric two-component magnetic turbulence. In the two-component model, we assume

$$\mathbf{B} = \mathbf{B_0} + \mathbf{b}(x, y, z), \tag{1}$$

where the mean field $\mathbf{B_0}$ is constant. We also use

$$\mathbf{B_0} = B_0\hat{\mathbf{z}}, \quad \mathbf{b} \perp \hat{\mathbf{z}}, \tag{2}$$

and the fluctuating field, of mean zero, is given by

$$\mathbf{b} = \mathbf{b}^{2D}(x,y) + \mathbf{b}^{slab}(z). \tag{3}$$

For brevity, we will refer to a quantity such as $\langle b^2 \rangle$ as the magnetic energy of the fluctuations, E, and define $b \equiv \sqrt{\langle b^2 \rangle}$. In general, we can write

$$\mathbf{b}^{2D}(x,y) = \nabla \times [a(x,y)\hat{\mathbf{z}}]. \tag{4}$$

The potential function $a(x,y)$ can be taken to be a random function fluctuating about a constant mean value, taken to be zero for convenience, with a well-behaved power spectrum $A(k_x, k_y)$ (Ruffolo et al. 2004).

In the absence of a slab component, the field lines for two-dimensional turbulence would move along curves of constant a, since equation (4) indicates that $\mathbf{b}^{2D} \perp \nabla a$. In three dimensions, such field lines are constrained to flux tubes that are "cylinders" in the mathematical sense of surfaces of constant $a(x,y)$. This can account for the repeated dropouts in observations of solar energetic particles from impulsive solar flares (Mazur et al. 2000; Ruffolo et al. 2003). A key feature that makes the two-component model of turbulence realistic and interesting is that the slab component imposes random perturbations on the field line motion, leading to mixing of field lines and wandering to regions of different $a(x,y)$ (see also Matthaeus et al. 1995).

Note that $B_z \equiv B_0$, so in this model it is impossible for a magnetic field line to backtrack in the z-direction, and the z-coordinate specifies a unique location along a magnetic field line. Therefore, we follow the standard practice of defining the field line diffusion coefficient in terms of the distance Δz:

$$\begin{aligned} D_x &= \frac{\langle (\Delta x)^2 \rangle}{2\Delta z} \\ D_y &= \frac{\langle (\Delta y)^2 \rangle}{2\Delta z}. \end{aligned} \tag{5}$$

For non-axisymmetric turbulence, we note that $\langle (\Delta x)^2 \rangle \neq \langle (\Delta y)^2 \rangle$. To obtain a non-axisymmetric slab field, we can explicitly set the parallel correlation length, ℓ_c, and rms slab magnitude, $b^{slab} \equiv \sqrt{\langle b^2 \rangle^{slab}}$, to be different in the x and y directions. For two-dimensional turbulence, the power spectrum $A(k_x, k_y)$ for the axisymmetric case depends only on $k_\perp = \sqrt{k_x^2 + k_y^2}$, i.e., it is constant along circles in (k_x, k_y) space. To consider non-axisymmetric

two-dimensional turbulence, we use a form that is instead constant along ellipses in (k_x, k_y) space (Figure 1). Note that our model incorporates the two key ways to violate axisymmetry: 1. a difference between the two "polarizations" (for the slab component), and 2. a difference between correlation scales in different directions (for the two-dimensional component).

Our analytic derivation of D_x and D_y follows those of Matthaeus et al. (1995) and Ruffolo et al. (2004) in assuming Corrsin's independence hypothesis (Corrsin 1959; Salu and Montgomery 1977; see also McComb 1990), Gaussian random walk distributions, and diffusive behavior. Computer simulations have been used to verify the validity of these assumptions for the field line random walk (Gray et al. 1996) and field line separation (Ruffolo et al. 2004) in two-component turbulence.

Following Jokipii & Parker (1969), we express the change in the x- and y-coordinates of a field line over a distance Δz along the mean magnetic field as

$$\Delta x \equiv x(\Delta z) - x(0) = \frac{1}{B_0}\int_0^{\Delta z} b_x[x(z'), y(z'), z']dz'$$
$$\Delta y \equiv y(\Delta z) - y(0) = \frac{1}{B_0}\int_0^{\Delta z} b_y[x(z'), y(z'), z']dz'. \quad (6)$$

The ensemble average of $(\Delta x)^2$ is then given by

$$\langle \Delta x^2 \rangle = \frac{1}{B_0^2}\int_0^{\Delta z}\int_0^{\Delta z} \langle b_x[x(z'), y(z'), z'] b_x[x(z''), y(z''), z'']\rangle dz'dz''$$
$$= \frac{1}{B_0^2}\int_0^{\Delta z}\int_0^{\Delta z} \langle b_x(x', y', z') b_x(x'', y'', z'')\rangle dz'dz'', \quad (7)$$

where we introduce the notation x' for $x(z')$, etc. We can also write

$$\langle \Delta x^2 \rangle = \frac{1}{B_0^2}\int_0^{\Delta z}\int_{-z'}^{\Delta z - z'} \langle b_x(x', y', z') b_x(x'', y'', z' + \Delta z')\rangle d\Delta z'dz', \quad (8)$$

where $\Delta z' \equiv z'' - z'$, and with the assumption of homogeneity,

$$\langle \Delta x^2 \rangle = \frac{1}{B_0^2}\int_0^{\Delta z}\int_{-z'}^{\Delta z - z'} \langle b_x(0,0,0) b_x(\Delta x', \Delta y', \Delta z')\rangle d\Delta z'dz', \quad (9)$$

where $\Delta x' \equiv x'' - x'$ and $\Delta y' \equiv y'' - y'$. By changing b_x to b_y we can obtain a similar formula for $\langle \Delta y^2 \rangle$.

Here we use Corrsin's hypothesis in position space and consider the Lagrangian correlation function $\langle b_x(x', y', z') b_x(x'', y'', z'')\rangle$ to be the Eulerian correlation function, $R_{xx} \equiv$

$\langle b_x(0,0,0)\dot{b_x}(x,y,z)\rangle$, weighted by the conditional probability of finding $(\Delta x', \Delta y')$ after a given $\Delta z'$:

$$\langle \Delta x^2 \rangle = \frac{1}{B_0^2} \int_0^{\Delta z} \int_{-z'}^{\Delta z - z'} \int_{-\infty}^{\infty} \int_{-\infty}^{\infty} R_{xx}(\Delta x', \Delta y', \Delta z') \times P(\Delta x'|\Delta z') P(\Delta y'|\Delta z') d\Delta x' d\Delta y' d\Delta z' dz'. \quad (10)$$

The formula for $\langle \Delta y^2 \rangle$ is similar:

$$\langle \Delta y^2 \rangle = \frac{1}{B_0^2} \int_0^{\Delta z} \int_{-z'}^{\Delta z - z'} \int_{-\infty}^{\infty} \int_{-\infty}^{\infty} R_{yy}(\Delta x', \Delta y', \Delta z') \times P(\Delta x'|\Delta z') P(\Delta y'|\Delta z') d\Delta x' d\Delta y' d\Delta z' dz'. \quad (11)$$

We assume the probabilities in equations (10) and (11) to be Gaussian distributions as

$$P(\Delta x'|\Delta z') = \frac{1}{\sqrt{2\pi\sigma_x^2}} \exp\left[-\frac{(\Delta x')^2}{2\sigma_x^2}\right]$$
$$P(\Delta y'|\Delta z') = \frac{1}{\sqrt{2\pi\sigma_y^2}} \exp\left[-\frac{(\Delta y')^2}{2\sigma_y^2}\right], \quad (12)$$

where σ_x^2 and σ_y^2 are the variances in x and y components. We apply the diffusion approximation for the variances, which are

$$\sigma_x^2 = \langle (\Delta x')^2 \rangle = 2D_x |\Delta z'|$$
$$\sigma_y^2 = \langle (\Delta y')^2 \rangle = 2D_y |\Delta z'|. \quad (13)$$

Thus equations (12) become

$$P(\Delta x'|\Delta z') = \frac{1}{\sqrt{4\pi D_x|\Delta z'|}} \exp\left[-\frac{(\Delta x')^2}{4D_x|\Delta z'|}\right]$$
$$P(\Delta y'|\Delta z') = \frac{1}{\sqrt{4\pi D_y|\Delta z'|}} \exp\left[-\frac{(\Delta y')^2}{4D_y|\Delta z'|}\right]. \quad (14)$$

Next we integrate equations (10) and (11) over $\Delta z'$ and z' and introduce the power spectra P_{xx} and P_{yy} as the Fourier transforms of the correlation functions R_{xx} and R_{yy}, respectively. Again using the diffusion approximation, we set $\langle \Delta x^2 \rangle = 2D_x \Delta z$ and $\langle \Delta y^2 \rangle = 2D_y \Delta z$. Finally, we obtain the coupled equations for D_x and D_y as

$$D_x = \frac{\langle \Delta x^2 \rangle}{2\Delta z} = \frac{1}{\sqrt{2\pi}} \frac{1}{B_0^2} \int_{-\infty}^{\infty} \frac{1 - \cos(k_z \Delta z)}{k_z^2 \Delta z} P_{xx}^{slab}(k_z) dk_z$$

$$
\begin{aligned}
& + \frac{1}{2\pi}\frac{1}{B_0^2}\int_{-\infty}^{\infty}\int_{-\infty}^{\infty}\frac{P_{xx}^{2D}(k_x,k_y)}{(D_x k_x^2 + D_y k_y^2)} \\
& \times \left\{1 - g\left[(D_x k_x^2 + D_y k_y^2)\Delta z\right]\right\} dk_x dk_y \\
D_y = \frac{\langle \Delta y^2 \rangle}{2\Delta z} &= \frac{1}{\sqrt{2\pi}}\frac{1}{B_0^2}\int_{-\infty}^{\infty}\frac{1-\cos(k_z\Delta z)}{k_z^2 \Delta z} P_{yy}^{slab}(k_z) dk_z \\
& + \frac{1}{2\pi}\frac{1}{B_0^2}\int_{-\infty}^{\infty}\int_{-\infty}^{\infty}\frac{P_{yy}^{2D}(k_x,k_y)}{(D_x k_x^2 + D_y k_y^2)} \\
& \times \left\{1 - g\left[(D_x k_x^2 + D_y k_y^2)\Delta z\right]\right\} dk_x dk_y, \qquad (15)
\end{aligned}
$$

where $g(u) \equiv (1 - e^{-u})/u$ behaves as a low-pass filter, i.e., $g(u) \approx 1$ for $u \ll 1$ and monotonically declines to zero as $u \to \infty$.

Following Ruffolo et al. (2004), when we choose a large Δz, equations (15) become

$$
\begin{aligned}
D_x - D_x^{slab} &= \frac{1}{2\pi}\frac{1}{B_0^2}\int_{-\infty}^{\infty}\int_{-\infty}^{\infty}\frac{P_{xx}^{2D}(k_x,k_y)}{(D_x k_x^2 + D_y k_y^2)} dk_x dk_y \\
D_y - D_y^{slab} &= \frac{1}{2\pi}\frac{1}{B_0^2}\int_{-\infty}^{\infty}\int_{\infty}^{\infty}\frac{P_{yy}^{2D}(k_x,k_y)}{(D_x k_x^2 + D_y k_y^2)} dk_x dk_y, \qquad (16)
\end{aligned}
$$

where

$$
D_x^{slab} = \sqrt{\frac{\pi}{2}}\frac{P_{xx}^{slab}(0)}{B_0^2} = \frac{\ell_x f_{sx} b^2}{B_0^2} \qquad (17)
$$

$$
D_y^{slab} = \sqrt{\frac{\pi}{2}}\frac{P_{yy}^{slab}(0)}{B_0^2} = \frac{\ell_y f_{sy} b^2}{B_0^2}. \qquad (18)
$$

Here ℓ_x and ℓ_y are the correlation lengths in the x and y directions, respectively, f_{sx} is the fraction of turbulent energy that is slab energy in the x direction, $f_{sx} = \langle b_x^2 \rangle^{slab}/\langle b^2 \rangle$, and similarly f_{sy} is the fraction that is slab energy in the y direction.

Equations (17) and (18), which correspond to the results of Jokipii & Parker (1968), make it clear how non-axisymmetry affects the field line random walk due to the slab component of turbulence. The effect on the two-dimensional component is not as clear, especially because $P_{xx}^{2D}(k_x,k_y)$ and $P_{yy}^{2D}(k_x,k_y)$ are not independent functions. From equation (4), which relates $\mathbf{b}^{2D}(x,y)$ to the potential function $a(x,y)$, we infer that $P_{xx}^{2D} = k_y^2 A$ and $P_{yy}^{2D} = k_x^2 A$, where $A(k_x,k_y)$ is the power spectrum of $a(x,y)$. Thus non-axisymmetry in the two-dimensional component of the turbulent magnetic field is generated by non-axisymmetry in $A(k_x,k_y)$.

For the axisymmetric case, $A(k_x,k_y)$ is constant along circles of constant $k_\perp = \sqrt{k_x^2 + k_y^2}$ in (k_x,k_y) space, so $A = A(k_\perp)$. For the non-axisymmetric case, we model the two-dimensional component by taking $A(k_x,k_y)$ to be constant along ellipses in (k_x,k_y) space

that have a major to minor axis ratio of β/α (see Figure 1). We refer to this ratio as the ellipticity parameter ξ, and Figure 2 shows examples of $A(x,y)$ and representations of the two-dimensional potential function $a(x,y)$ for $\xi = 1$ (axisymmetric case) and $\xi = 4$ (a non-axisymmetric case). Note that using $\xi \neq 1$ stretches the "islands" of constant $a(x,y)$. Now we write $k'_x = k_x/\alpha$, $k'_y = k_y/\beta$, and $k'_\perp = \sqrt{k'^2_x + k'^2_y} = \sqrt{k^2_x/\alpha^2 + k^2_y/\beta^2}$, and assume $A = A(k'_\perp)$. This yields

$$\begin{aligned} D_x - D_x^{slab} &= \frac{1}{2\pi}\frac{1}{B_0^2}\int_{-\infty}^{\infty}\int_{-\infty}^{\infty}\frac{\beta^2 k'^2_y A(k'_\perp)}{(D_x\alpha^2 k'^2_x + D_y\beta^2 k'^2_y)}d(\alpha k'_x)d(\beta k'_y) \\ D_y - D_y^{slab} &= \frac{1}{2\pi}\frac{1}{B_0^2}\int_{-\infty}^{\infty}\int_{-\infty}^{\infty}\frac{\alpha^2 k'^2_x A(k'_\perp)}{(D_x\alpha^2 k'^2_x + D_y\beta^2 k'^2_y)}d(\alpha k'_x)d(\beta k'_y). \end{aligned} \tag{19}$$

Next, we write equations (19) in polar coordinates $k'_\perp$ and θ such that $k'_x = k'_\perp \cos\theta$ and $k'_y = k'_\perp \sin\theta$:

$$\begin{aligned} D_x - D_x^{slab} &= \frac{\alpha\beta}{2\pi B_0^2}\int_0^{2\pi}\int_0^{\infty}\frac{\beta^2 k'^2_\perp \sin^2\theta A(k'_\perp)}{(D_x\alpha^2 k'^2_\perp\cos^2\theta + D_y\beta^2 k'^2_\perp\sin^2\theta)}k'_\perp dk'_\perp d\theta \\ &= \frac{\alpha\beta}{2\pi B_0^2 D_x}\frac{\beta^2}{\alpha^2}\int_0^{\infty}A(k'_\perp)k'_\perp dk'_\perp\int_0^{2\pi}\frac{1}{\cot^2\theta + \frac{\beta^2}{\alpha^2}\frac{D_y}{D_x}}d\theta \\ D_y - D_y^{slab} &= \frac{\alpha\beta}{2\pi B_0^2}\int_0^{2\pi}\int_0^{\infty}\frac{\alpha^2 k'^2_\perp\cos^2\theta A(k'_\perp)}{(D_x\alpha^2 k'^2_\perp\cos^2\theta + D_y\beta^2 k'^2_\perp\sin^2\theta)}k'_\perp dk'_\perp d\theta \\ &= \frac{\alpha\beta}{2\pi B_0^2 D_x}\int_0^{\infty}A(k'_\perp)k'_\perp dk'_\perp\int_0^{2\pi}\frac{1}{1 + \frac{\beta^2}{\alpha^2}\frac{D_y}{D_x}\tan^2\theta}d\theta. \end{aligned} \tag{20}$$

Note that

$$\int_0^{\infty}[1/(\cot^2\theta + \rho^2)]d\theta = 2\pi/[\rho(\rho+1)] \tag{21}$$

and

$$\int_0^{\infty}[1/(1 + \rho^2\tan^2\theta)]d\theta = 2\pi/(\rho+1), \tag{22}$$

where $\rho = (\beta/\alpha)\sqrt{D_y/D_x}$ in our integrals. Then we obtain

$$\begin{aligned} D_x - D_x^{slab} &= \left(\frac{\alpha\beta}{B_0^2}\int_0^{\infty}A(k'_\perp)k'_\perp dk'_\perp\right)\frac{\beta^2}{\alpha^2 D_x}\frac{1}{\frac{\beta}{\alpha}\sqrt{\frac{D_y}{D_x}}\left(1 + \frac{\beta}{\alpha}\sqrt{\frac{D_y}{D_x}}\right)} \\ D_y - D_y^{slab} &= \left(\frac{\alpha\beta}{B_0^2}\int_0^{\infty}A(k'_\perp)k'_\perp dk'_\perp\right)\frac{1}{D_x}\frac{1}{\left(1 + \frac{\beta}{\alpha}\sqrt{\frac{D_y}{D_x}}\right)}. \end{aligned} \tag{23}$$

Let us define I to be the term in parentheses:

$$I = \frac{\alpha\beta}{B_0^2} \int_0^\infty A(k'_\perp) k'_\perp dk'_\perp. \tag{24}$$

Transforming $k'_\perp$ back to k_x and k_y,

$$\begin{aligned} I &= \frac{1}{2\pi B_0^2} \int_{-\infty}^{\infty} \int_{-\infty}^{\infty} A(k_x, k_y) dk_x dk_y \\ &= \frac{\langle a^2 \rangle}{B_0^2} = \left(\tilde{\lambda} \frac{b^{2D}}{B_0} \right)^2 \\ &= 2(D_\perp^{2D})^2, \end{aligned} \tag{25}$$

where $\tilde{\lambda}$ is called the "ultrascale" (Matthaeus et al. 1995). Combining equations (23) and (24), we obtain the coupled biquadratic equations for the field line random walk in a non-axisymmetric two-component model of magnetic turbulence:

$$\begin{aligned} \left(D_x - D_x^{slab}\right) \left(D_y + \frac{\alpha}{\beta} \sqrt{D_x D_y} \right) &= I \\ \left(D_y - D_y^{slab}\right) \left(D_x + \frac{\beta}{\alpha} \sqrt{D_x D_y} \right) &= I. \end{aligned} \tag{26}$$

In terms of the ellipticity parameter $\xi = \beta/\alpha$ we have

$$\begin{aligned} \left(D_x - D_x^{slab}\right) \left(D_y + \frac{\sqrt{D_x D_y}}{\xi} \right) &= I \\ \left(D_y - D_y^{slab}\right) \left(D_x + \xi \sqrt{D_x D_y} \right) &= I. \end{aligned} \tag{27}$$

These equations are straightforward to solve numerically for a given case of interest, and in the next section we derive closed-form solutions for certain limiting cases.

3. Interpretation

To solve the coupled biquadratic equations (27), a "user" of the calculation needs to specify certain physical inputs:

B_0, the mean magnetic field,

b, the root-mean-squared turbulent magnetic field,

f_s, the slab fraction of turbulent energy,

$\eta^2 \equiv f_{sx}/f_{sy}$, the slab anisotropy,

ℓ_x, the correlation length of b_x^{slab},

ℓ_y, the correlation length of b_y^{slab},

$\tilde{\lambda}$, the ultrascale (of two-dimensional turbulence), and

ξ, the ellipticity parameter.

Actually, instead of providing both b and B_0, it is sufficient to specify only their ratio. The two anisotropy parameters η and ξ are quite distinct physically: We will show shortly that ξ is also the anisotropy of the field line diffusion coefficients for the two-dimensional component alone: $\xi^2 = D_x^{2D}/D_y^{2D}$. In terms of these inputs, the quantities in equations (27) are given as

$$D_x^{slab} = \frac{\eta^2}{\eta^2+1}\frac{\ell_x f_s b^2}{B_0^2} \tag{28}$$

$$D_y^{slab} = \frac{1}{\eta^2+1}\frac{\ell_y f_s b^2}{B_0^2}. \tag{29}$$

$$I = (1-f_s)\left(\tilde{\lambda}\frac{b}{B_0}\right)^2, \tag{30}$$

and from equation (25) we have $I = 2(D_\perp^{2D})^2$, so

$$D_\perp^{2D} = \sqrt{\frac{1-f_s}{2}}\,\tilde{\lambda}\,\frac{b}{B_0}. \tag{31}$$

Note that D_x^{slab} and D_y^{slab} depend on $(b/B_0)^2$, whereas $D_\perp^{2D} \propto b/B_0$ (see also Taylor & McNamara 1971).

Let us stress that the results in §2 apply for general and independent functional forms of $P_{xx}^{slab}(k_z)$, $P_{yy}^{slab}(k_z)$, and $A(k'_\perp)$. For the slab fluctuations, we allow a general polarization in the sense that x- and y-polarizations have independent power spectra, and we see that the calculation depends only on the product $\ell_i f_{si}$, where $i = x$ or y. For the two-dimensional fluctuations, we take $A(k_x, k_y)$ to be stretched in one direction relative to the axisymmetric configuration (Figures 1 and 2). Thus the slab anisotropy η and ellipticity ξ represent physically distinct types of non-axisymmetry.

In many applications, direct measurements of the physical inputs are not available, so one must make educated guesses or *ad hoc* approximations. Here we present solutions of

the general equations (27) for specific limits and approximations. Naturally, the simplest approximation is that either slab or two-dimensional turbulence can be neglected. For the case where two-dimensional turbulence is absent, we have $f_s = 1$, $I = 0$, $D_x = D_x^{slab}$, and $D_y = D_y^{slab}$, so we recover the Jokipii & Parker (1968) results for slab turbulence as in equations (28) and (29).

Next, consider the limit where the slab fraction goes to zero. It is useful to define the geometric mean of overall diffusion coefficients, $D_\perp \equiv \sqrt{D_x D_y}$, and an anisotropy of overall diffusion coefficients, $\delta \equiv \sqrt{D_x/D_y}$. Setting $D_x^{slab} = D_y^{slab} = 0$, equations (27) give

$$\begin{aligned} D_\perp^2 \left(1 + \frac{\delta}{\xi}\right) &= I \\ D_\perp^2 \left(1 + \frac{\xi}{\delta}\right) &= I, \end{aligned} \tag{32}$$

which are only satisfied for $\delta = \xi$, giving $D_\perp = \sqrt{I/2} = D_\perp^{2D}$ as in Matthaeus et al. (1995). Therefore,

$$\begin{aligned} D_x &= \delta D_\perp = \xi D_\perp^{2D} \\ D_y &= \frac{D_\perp}{\delta} = \frac{D_\perp^{2D}}{\xi} \end{aligned} \tag{33}$$

and we can indeed interpret ξ as the anisotropy of the field line random walk for two-dimensional turbulence, $\xi = \sqrt{D_x^{2D}/D_y^{2D}}$.

Now suppose that both the slab and two-dimensional components are present. If η and ξ are not known, a simple approximation is to set them equal ($\eta = \xi$). Let us also set $\ell_x = \ell_y = \ell$, which along with equations (28) and (29) implies that $\eta = \sqrt{D_x^{slab}/D_y^{slab}}$. Then from an argument similar to that for the pure two-dimensional case, it can be shown that $\delta = \xi$ as well. Therefore, equations (27) decouple to these two equations:

$$\begin{aligned} \left(D_x - D_x^{slab}\right)\left(\frac{D_x}{\xi^2}\right) &= \frac{I}{2} \\ \left(D_y - D_y^{slab}\right)\left(\xi^2 D_y\right) &= \frac{I}{2}. \end{aligned} \tag{34}$$

The solutions for this case are

$$\begin{aligned} D_x &= \frac{1}{2}\left[D_x^{slab} + \sqrt{(D_x^{slab})^2 + 4\left(D_x^{2D}\right)^2}\right] \\ D_y &= \frac{1}{2}\left[D_y^{slab} + \sqrt{(D_y^{slab})^2 + 4\left(D_y^{2D}\right)^2}\right], \end{aligned} \tag{35}$$

which is the same as the formula obtained by Matthaeus et al. (1995) but now applied separately to D_x and D_y quantities. In terms of the physical inputs, we have

$$D_x = \frac{1}{2}\left[\frac{\xi^2}{\xi^2+1}\frac{\ell f_s b^2}{B_0^2} + \sqrt{\left(\frac{\xi^2}{\xi^2+1}\frac{\ell f_s b^2}{B_0^2}\right)^2 + 4\xi^2\left(D_\perp^{2D}\right)^2}\right]$$

$$D_y = \frac{1}{2}\left[\frac{1}{\xi^2+1}\frac{\ell f_s b^2}{B_0^2} + \sqrt{\left(\frac{1}{\xi^2+1}\frac{\ell f_s b^2}{B_0^2}\right)^2 + 4\frac{\left(D_\perp^{2D}\right)^2}{\xi^2}}\right]. \quad (36)$$

Now further suppose that the turbulence is extremely non-axisymmetric, i.e., that all other input values are fixed but η and ξ both tend to 0 or both tend to ∞. Then from equations (36) it can be seen that the two-dimensional contribution dominates. That is, when ξ tends to zero, $D_x \to \xi D_\perp^{2D}$ and $D_y \to D_\perp^{2D}/\xi$. Similarly, as ξ goes to ∞, we again have $D_x \to \xi D_\perp^{2D}$ and $D_y \to D_\perp^{2D}/\xi$. Such extreme non-axisymmetry might occur in the outer heliosphere if field fluctuations are "frozen in" the solar wind as it expands very differently in the two perpendicular directions.

Now let us return to the general case of any possible input parameters. For convenience in analyzing the coupled equations (27), we can rewrite all variables to compare with the two-dimensional values, yielding

$$D'_\perp = \frac{D_\perp}{D_\perp^{2D}} \qquad D_\perp^{s\,\prime} = \frac{D_\perp^{slab}}{D_\perp^{2D}} \quad (37)$$

$$\delta' = \frac{\delta}{\xi} = \frac{\sqrt{D_x/D_y}}{\sqrt{D_x^{2D}/D_y^{2D}}} \quad (38)$$

$$\eta' = \frac{\eta\sqrt{\ell_x/\ell_y}}{\xi} = \frac{\sqrt{D_x^{slab}/D_y^{slab}}}{\sqrt{D_x^{2D}/D_y^{2D}}}, \quad (39)$$

where we define $D_\perp$, $D_\perp^{2D}$, and $D_\perp^{slab}$ as the geometric means $\sqrt{D_x D_y}$, $\sqrt{D_x^{2D} D_y^{2D}}$, and $\sqrt{D_x^{slab} D_y^{slab}}$, respectively. Now equations (27) become two coupled equations with two unknown parameters $D'_\perp$ and δ':

$$D'_\perp\left(\frac{1}{\delta'}+1\right)\left(\delta' D'_\perp - \eta' D_\perp^{s\,\prime}\right) = 2$$

$$D'_\perp(\delta'+1)\left(\frac{D'_\perp}{\delta'} - \frac{D_\perp^{s\,\prime}}{\eta'}\right) = 2. \quad (40)$$

Note that $D_\perp^{s\,\prime}$ and η' are known in terms of the input parameters via equations (28) to (30) (recalling that $D_\perp^{2D} = \sqrt{I/2}$). In particular,

$$D_\perp^{s\,\prime} = \frac{\sqrt{2\ell_x\ell_y}}{\widetilde{\lambda}} \frac{\eta}{\eta^2+1} \frac{f_s}{\sqrt{1-f_s}} \frac{b}{B_0} \tag{41}$$

$$\eta' D_\perp^{s\,\prime} = \frac{\sqrt{2}\ell_x}{\widetilde{\lambda}} \frac{\eta^2}{\eta^2+1} \frac{1}{\xi} \frac{f_s}{\sqrt{1-f_s}} \frac{b}{B_0} \tag{42}$$

$$\frac{D_\perp^{s\,\prime}}{\eta'} = \frac{\sqrt{2}\ell_y}{\widetilde{\lambda}} \frac{\xi}{\eta^2+1} \frac{f_s}{\sqrt{1-f_s}} \frac{b}{B_0}. \tag{43}$$

Now suppose that $\eta \to \infty$, while ξ is fixed. Then the terms $D_\perp^{s\,\prime}/\eta'$ and $\eta' D_\perp^{s\,\prime}$ go to zero and a constant, respectively. The coupled equations become

$$D'_\perp \left(\frac{1}{\delta'} + 1\right) (\delta' D'_\perp - \eta' D_\perp^{s\,\prime}) = 2 \tag{44}$$

$$D'_\perp (\delta' + 1) \left(\frac{D'_\perp}{\delta'}\right) = 2. \tag{45}$$

For this case, if $\eta' D_\perp^{s\,\prime} \ll 1$, which implies $D_x^{slab} \ll D_x^{2D}$, the equations above are

$$D'_\perp \left(\frac{1}{\delta'} + 1\right) (\delta' D'_\perp) = 2$$

$$D'_\perp (\delta' + 1) \left(\frac{D'_\perp}{\delta'}\right) = 2.$$

The solutions are $D'_\perp \approx 1$ and $\delta' \approx 1$. That is, when $\eta \to \infty$ and $D_x^{slab} \ll D_x^{2D}$, the diffusion coefficients tend to two-dimensional values ($D_i \approx D_i^{2D}$). If instead $\eta' D_\perp^{s\,\prime} \gg 1$, which implies $D_x^{slab} \gg D_x^{2D}$, then considering equation (44) we know that $\delta' D'_\perp$ must be greater than $\eta' D_\perp^{s\,\prime}$ because the left hand side of that equation needs to be positive. Thus $\delta' > \eta' D_\perp^{s\,\prime}/D'_\perp$. From equation (45), we can write

$$\delta' = \frac{D_\perp'^2}{2 - D_\perp'^2} \tag{46}$$

and also

$$D'_\perp = \sqrt{\frac{2}{1 + 1/\delta'}}. \tag{47}$$

Here we note from (47) that $0 < D'_\perp < \sqrt{2}$, so $\delta' \gg 1$. This in turn implies $D'_\perp \approx \sqrt{2}$, and then equation (44) implies that $\delta' D'_\perp \approx \eta' D_\perp^{s\,\prime}$ and $\delta' \approx \eta' D_\perp^{s\,\prime}/\sqrt{2}$. Converting these to diffusion coefficients, the solutions for the case where $\eta \to \infty$ and $D_x^{slab} \gg D_x^{2D}$ are $D_x \approx D_x^{slab}$ and $D_y \approx 2D_x^{2D} D_y^{2D}/D_x^{slab}$, which is much lower than D_y^{2D}. Paradoxically, the

increased slab turbulence in the x-direction leads to *decreased* y-diffusion. That means that when D_x^{slab} makes D_x very large, it decorrelates the random flights in the y-direction and also decreases the mean free path in the y-direction and D_y. An analogous result in the case of field line separation was found by Ruffolo et al. (2004).

If η instead goes to zero, the roles of x- and y-components are reversed. That is if $D_y^{slab} \ll D_y^{2D}$, then the diffusion coefficients tend to two-dimensional values. If, on the other hand, $D_y^{slab} \gg D_y^{2D}$, then $D_y \approx D_y^{slab}$ and $D_x \approx 2D_x^{2D}D_y^{2D}/D_y^{slab}$, which is much lower than D_x^{2D}.

Finally, we consider the case where $\xi \to \infty$ for fixed η. It can be shown that if $D_\perp^{slab} \gg D_\perp^{2D}$, then $D_i \approx D_i^{slab}$. If $D_\perp^{slab} \ll D_\perp^{2D}$, then $D_y \approx D_y^{slab}$ while $D_x \approx 2D_x^{2D}D_y^{2D}/D_y^{slab}$, which is again much lower than D_x^{2D}.

4. Numerical Confirmation

To confirm the conclusions of these analytic calculations, we have also performed computer simulations of the field line random walk in non-axisymmetric two-component turbulence. While the simulations inevitably involve some discretization and statistical errors, they do avoid the key assumptions of the analytic work (Corrsin's hypothesis and Gaussian probability distributions) and thus provide an independent check of their validity. For axisymmetric turbulence, these assumptions have been computationally verified for the field line random walk (Gray et al. 1996) and for field line separation (Ruffolo et al. 2004) to within $\sim 15\%$.

In order to simulate non-axisymmetric turbulence, we construct the power spectra differently in the x- and y-directions. For slab turbulence, we set the power spectrum for simulations as

$$P_{ii}^{slab}(k_z) = \frac{C_i^{slab}}{[1+(k_z\lambda_i)^2]^{5/6}}, \quad (i = x, y), \tag{48}$$

where C_i^{slab} is a normalization constant of the i-component, set so as to obtain the desired slab turbulence energy, and λ_i is the parallel correlation scale of the i-component, which is directly related to the correlation length ℓ_i. For the two-dimensional component, we instead specify the power spectrum $A(k_x, k_y)$ because as discussed in §2, the power spectra P_{xx}^{2D} and P_{yy}^{2D} can be written as

$$\begin{aligned} P_{xx}^{2D}(k_x, k_y) &= k_y^2 A(k'_\perp) \\ P_{yy}^{2D}(k_x, k_y) &= k_x^2 A(k'_\perp), \end{aligned} \tag{49}$$

where $k'_\perp$ is defined in §2. The function of A that we use for simulations is

$$A(k'_\perp) = \frac{C^{2D}}{[1+(k'_\perp \ell_\perp)^2]^{7/3}}. \tag{50}$$

This form of the two-dimensional spectrum also permits the axisymmetric case when $\xi = 1$. These forms of the slab and two-dimensional power spectra are consistent with a Kolmogorov power-law in the omnidirectional power spectrum at high wavenumber (Ruffolo et al. 2004), while rolling over to constant values of P_{ii}^{slab} and A at small wavenumbers. They provide a reasonable description of observed power spectra in interplanetary space over the energy-containing and inertial ranges of turbulence (Jokipii & Coleman 1968; Bieber et al. 1996).

Now we have the spectra of magnetic turbulence. The relations between the magnetic field fluctuations and power spectra are

$$b_x^{slab}(k_z) = \sqrt{P_{xx}^{slab}} e^{i\phi(k_z)} \tag{51}$$

$$b_y^{slab}(k_z) = \sqrt{P_{yy}^{slab}} e^{i\phi(k_z)} \tag{52}$$

$$b_x^{2D}(k_x,k_y) = -ik_y \sqrt{A(k_x,k_y)} e^{i\phi(k_x,k_y)} \tag{53}$$

$$b_y^{2D}(k_x,k_y) = ik_x \sqrt{A(k_x,k_y)} e^{i\phi(k_x,k_y)}, \tag{54}$$

where ϕ is an independent random phase for each Fourier mode. After we generate the magnetic fluctuations in **k**-space, we use inverse Fourier transforms to convert them to real space. Now we have a representation of two-dimensional and slab fluctuations in the simulation box. Next, the field line equations

$$\frac{dx}{dz} = \frac{b_x(x,y,z)}{B_0} \qquad \frac{dy}{dz} = \frac{b_y(x,y,z)}{B_0} \tag{55}$$

are solved by a fourth-order Runge-Kutta method with adaptive step size control (Press et al. 1992).

After we get the positions of each field line, yielding the diffusion coefficients, values of $\langle \Delta x^2 \rangle$ and $\langle \Delta y^2 \rangle$ are averaged over the set of field lines at Δz much greater than the correlation length. Then we determine $D_x = \langle \Delta x^2 \rangle / (2\Delta z)$ and $D_y = \langle \Delta y^2 \rangle / (2\Delta z)$. To ensure that our set of field lines properly samples the ensemble of magnetic fluctuations and to avoid periodicity effects, we randomly set starting points of the field lines in the simulation box, change the realization of the two-dimensional component for every simulation, and trace the field lines to only a few percent of the box length L_z.

To verify the theory, we perform the simulations for three cases. For the first case, we confirm the theory for non-axisymmetric slab turbulence with no two-dimensional component. The results from simulations are compared with the discrete theory, i.e., the solution

to equations (27) to (30) in which the integrals used to determine ℓ_x, ℓ_y, $\langle b^2 \rangle^{slab}$, and $\widetilde{\lambda}$ are replaced by discrete sums over the actual Fourier modes used in the simulations. This helps reduce the effect of discrete Fourier modes on the comparison, and allows us to better check the assumptions underlying the theory. We set $L_x = L_y = L_z = 100,000\lambda_x$ and trace the field lines over only 2.5% of L_z. The number of grid points is $N_z = 2^{22} \approx 4$ million. The parameters governing anisotropy for this case are f_{sx}/f_{sy}, λ_x, and λ_y. In the axisymmetric case, we usually set $\lambda_x = \lambda_y = 1$ and $f_{sx} = f_{sy} = 0.5$, where $f_{sx} = \langle b_x^2 \rangle^{slab}/\langle b^2 \rangle$ and $f_{sy} = \langle b_y^2 \rangle^{slab}/\langle b^2 \rangle$. If we change these three parameters to other values, the system becomes non-axisymmetric. In this simulation we set b/B_0=0.5 as a constant for all runs. The simulation results are shown in Table 1, and they match the discrete theory quite closely.

In the second case, we simulate field lines in two-component models that are non-axisymmetric only in the two-dimensional component but axisymmetric in the slab component ($D_x^{slab} = D_y^{slab}$). We maintain $f_{sx} = f_{sy} = 0.5 f_s$ and $\lambda_x = \lambda_y = 1$, and vary only the ellipticity ξ of $A(k_x, k_y)$. Therefore, we should have a constant $D_x^{slab} = D_y^{slab}$ for all of these runs. Moreover we set $\ell_\perp = 1$ and $b/B_0 = 0.5$ and perform two sets of simulations, for $E^{slab} : E^{2D} = 20 : 80$, a good approximation for the solar wind (Bieber et al. 1994, 1996), and for $E^{slab} : E^{2D} = 80 : 20$. In the simulations, we trace 1,000 field lines in the large box with $L_z = 100,000\lambda_x$ and $L_x = L_y = 200\lambda_x$. The numbers of grid points are $N_x = N_y = 4,096$ and $N_z = 2^{22}$. Tables 2 and 3 indicate the numerical and theoretical values and their differences when we vary the ellipticity ξ for $E^{slab} : E^{2D} = 20 : 80$ and $80 : 20$. The theoretical values and numerical results for those two cases are also plotted in Figures 3 and 4, respectively. For $E^{slab} : E^{2D} = 20{:}80$, we add two columns in Table 2 with kurtosis values of each component, $\kappa_x \equiv \langle \Delta x^4 \rangle / \langle \Delta x^2 \rangle^2$ and $\kappa_y \equiv \langle \Delta y^4 \rangle / \langle \Delta y^2 \rangle^2$, to test for similarity to Gaussian distributions, which have a kurtosis of 3. We conclude that all kurtosis values are consistent with those of Gaussian distributions.

Finally, to be sure that the theory also works for various cases in which both the slab and two-dimensional turbulence are non-axisymmetric, we independently vary the parameters that cause non-axisymmetry of the two-component turbulent field. We use the box size and other parameters as previously but vary f_{sx}/f_s, λ_x, λ_y, and ξ. Table 4 shows the results, which indicate reasonable agreement between simulations and the discrete theory.

5. Summary

We analytically derive the field-line diffusion coefficients in the directions x and y, perpendicular to the mean field direction z, for non-axisymmetric, two-component (2D + slab) turbulence, with variances transverse to the mean magnetic field, and adopting the

additional assumptions of spatial homogeneity, the diffusion approximation, and Corrsin's independence hypothesis. The validity of the diffusion approximation and Corrsin's hypothesis is verified by numerical simulations that do not rely on these assumptions. The analytic results are non-perturbative in the sense that neither the turbulent energy of the slab or the 2D component is constrained to be small. The results also allow general and independent functional forms for the slab and 2D power spectra.

We can see that the numerical results and theory are in quite good agreement. For pure non-axisymmetric slab turbulence, the simulations agree very well with the theory, with differences less than 3% (Table 1). It is interesting to note the discrepancy between simulations and theory when $E_{slab} : E_{2D} = 20 : 80$ (the energy ratio in the solar wind) and the field is non-axisymmetric only in the two-dimensional component (see Figure 3 and Table 2). This is large (9%-13%) when ξ is near 1 and it drops when $\xi \gg 1$ and $\xi \ll 1$. Moreover, the discrepancy in the direction that gives a large diffusion coefficient is always greater than that in the direction that gives a small value. When we decrease the fraction of turbulent energy in the two-dimensional component to 20% ($E_{slab} : E_{2D} = 80 : 20$; see Figure 4 and Table 3), the differences between theory and numerical results decrease. It seems that the two-dimensional turbulent energy affects the discrepancy between theory and simulations. However, the differences are still within 15%, which is similar that obtained by Gray et al. (1996). Furthermore, the theory is also verified in the case where both slab and two-dimensional turbulence are non-axisymmetric (Table 4).

The two-component model considered here is a particular case of anisotropic turbulence, in which power in **k**-space is concentrated along the parallel (k_z) axis and along the perpendicular (k_x, k_y) plane, which has been shown to provide a useful description of solar wind turbulence and associated particle transport phenomena Matthaeus et al. (1990); Bieber et al. (1994, 1996). For slab turbulence, we allow non-axisymmetry in the form of independent power spectra in the x- and y-directions, i.e., a general polarization. For two-dimensional turbulence, one can have non-axisymmetry in terms of stretching in one direction, so we consider a power spectrum $A(k_x, k_y)$ of the potential function that is constant along ellipses in (k_x, k_y). Some previous studies of non-axisymmetric turbulence (e.g., Pommois et al. 1999, 2001) have instead considered an "ellipsoidal" power spectrum with no polarization and turbulent energy that is constant along ellipsoids in **k**-space, which has the advantage of including oblique wavevectors, and the disadvantages that analytic calculations are more difficult and certain quantities cannot be varied independently, such as P_{ii} as $\mathbf{k} \rightarrow 0$ along different directions. The model differences are sufficiently great that we defer a proper comparison for future work.

The solution for the diffusion coefficients in our model of non-axisymmetric two-component

turbulence is in the simple form of coupled biquadratic equations. We also show closed-form and limiting expressions for special cases of interest. In some cases there is a counter-intuitive result that enhanced fluctuations in one direction lead to decreased diffusion in other direction. This is because the long random flights in one direction tend to decorrelate the turbulence in the other direction. It is shown that extreme non-axisymmetry always leads to diffusion coefficients proportional to the root-mean-squared two-dimensional fluctuation (i.e., proportional to b/B_0). Since strong non-axisymmetry might be expected in the outer heliosphere as the solar wind stretches differently in the two perpendicular (non-azimuthal) directions, this result is relevant to the heliospheric transport of charged particles, such as solar modulation of galactic cosmic rays.

This research was partially supported by a Basic Research Grant and a Royal Golden Jubilee Fellowship from the Thailand Research Fund, the Rachadapisek Sompoj Fund of Chulalongkorn University, and the NASA Sun-Earth Connections Theory Program (grant NAG 5-8134).

REFERENCES

Belcher, J. W., & Davis, L., Jr. 1971, J. Geophys. Res., 76, 3534

Bieber, J. W., Matthaeus, W. H., Smith, C. W., Wanner, W., Kallenrode, M.-B., & Wibberenz, G. 1994, ApJ, 420, 294

Bieber, J. W., Wanner, W., & Matthaeus, W. H. 1996, J. Geophys. Res., 101, 2511

Burger, R. A., & Hattingh, M. 1998, ApJ, 505, 244

Chuychai, P., Ruffolo, D., Matthaeus, W. H., & Rowlands, G. 2005, ApJ, 633, L49

Corrsin, S. 1959, in Advances in Geophysics, v. 6, Atmospheric Diffusion and Air Pollution, eds. F. Frenkel and P. Sheppard (New York: Academic Press), 161

Dasso, S., Milano, L. J., Matthaeus, W. H., & Smith, C. W. 2005, ApJ, 635, L181

Gray, P. C., Pontius, D. H., Jr., & Matthaeus, W. H. 1996, Geophys. Res. Lett., 23, 965

Isichenko, M. B. 1991a, Plasma Phys. Controlled Fusion, 33, 795

Isichenko, M. B. 1991b, Plasma Phys. Controlled Fusion, 33, 809

Jokipii, J. R. 1966, ApJ, 146, 480

Jokipii, J. R. 1973, ApJ, 182, 585

Jokipii, J. R., & Coleman, P. J. 1968, J. Geophys. Res., 73, 5495

Jokipii, J. R., Kóta, J., Giacalone, J., Horbury, T. S., & Smith, E. J. 1995, Geophys. Res. Lett., 22, 3385

Jokipii, J. R., & Parker, E. N. 1968, Phys. Rev. Lett., 21, 44

Jokipii, J. R., & Parker, E. N. 1969, ApJ, 155, 777

Leamon, R. J., Smith, C. W., & Ness, N. F. 1998, Geophys. Res. Lett., 25, 2505

Matthaeus, W. H., Goldstein, M. L., & Roberts, D. A. 1990, J. Geophys. Res., 95, 20673

Matthaeus, W. H., Gray, P. C., Pontius, D. H., Jr., & Bieber, J. W. 1995, Phys. Rev. Lett., 75, 2136

Mazur, J. E., Mason, G. M., Dwyer, J. R., Giacalone, J., Jokipii, J. R., and Stone, E. C. 2000, ApJ, 532, L79

McComb, W. D. 1990, The Physics of Fluid Turbulence (Oxford: Clarendon)

Parker, E. N. 1958, ApJ, 128, 664

Pommois, P., Veltri, P., & Zimbardo, G. 1999, Phys. Rev. E, 59, 2244

Pommois, P., Veltri, P., & Zimbardo, G. 2001, Phys. Rev. E, 63, 066405

Press, W. H., Teukolsky, S. A., Vetterling, W. T., & Flannery, B. P. 1992, Numerical Recipes in FORTRAN: The Art of Scientific Computing (Cambridge: Cambridge Univ. Press)

Rechester, A. B., & Rosenbluth, M. M. 1978, Phys. Rev. Lett., 40, 38

Ruffolo, D., Matthaeus, W. H., & Chuychai, P. 2003, ApJ, 597, L169

Ruffolo, D., Matthaeus, W. H., & Chuychai, P. 2004, ApJ, 614, 420

Salu, Y., and Montgomery, D. C. 1977, Phys. Fluids, 20, 1

Smith, C. W., Mullan, D. J., & Ness, N. F. 2004, J. Geophys. Res., 109, A01111

Smith, C. W., Mullan, D. J., Ness, N. F., Skoug, R. M., & Steinberg, J. 2001, J. Geophys. Res., 106, 18625

Taylor, J. B., & McNamara, B. 1971, Phys. Fluids, 14, 1492

Wang, H.-D., Vlad, M., Vanden Eijnden, E., Spineanu, F., Misguich, J. H., & Balescu, R. 1995, Phys. Rev. E, 51, 4844

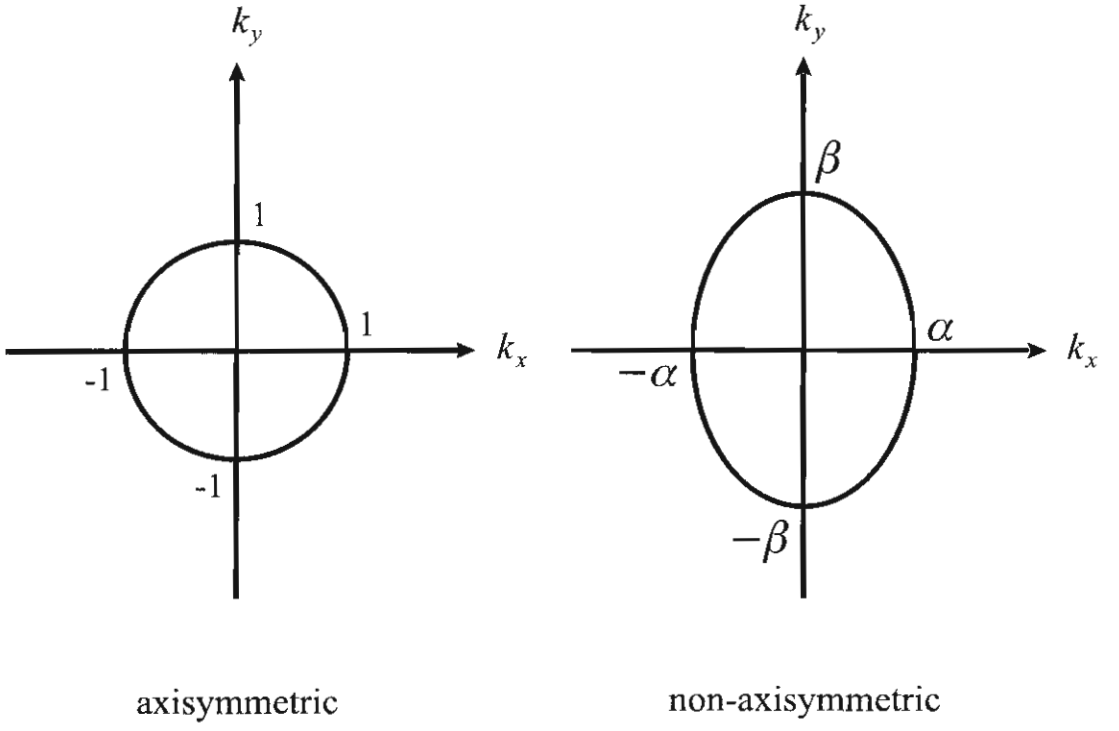

Fig. 1.— Contours of constant power $A(k_x, k_y)$ of the two-dimensional potential function for the axisymmetric model and for our non-axisymmetric model. To maintain the same turbulent energy, we can set $\alpha = 1/\sqrt{\xi}$ and $\beta = \sqrt{\xi}$, where ξ is an ellipticity parameter.

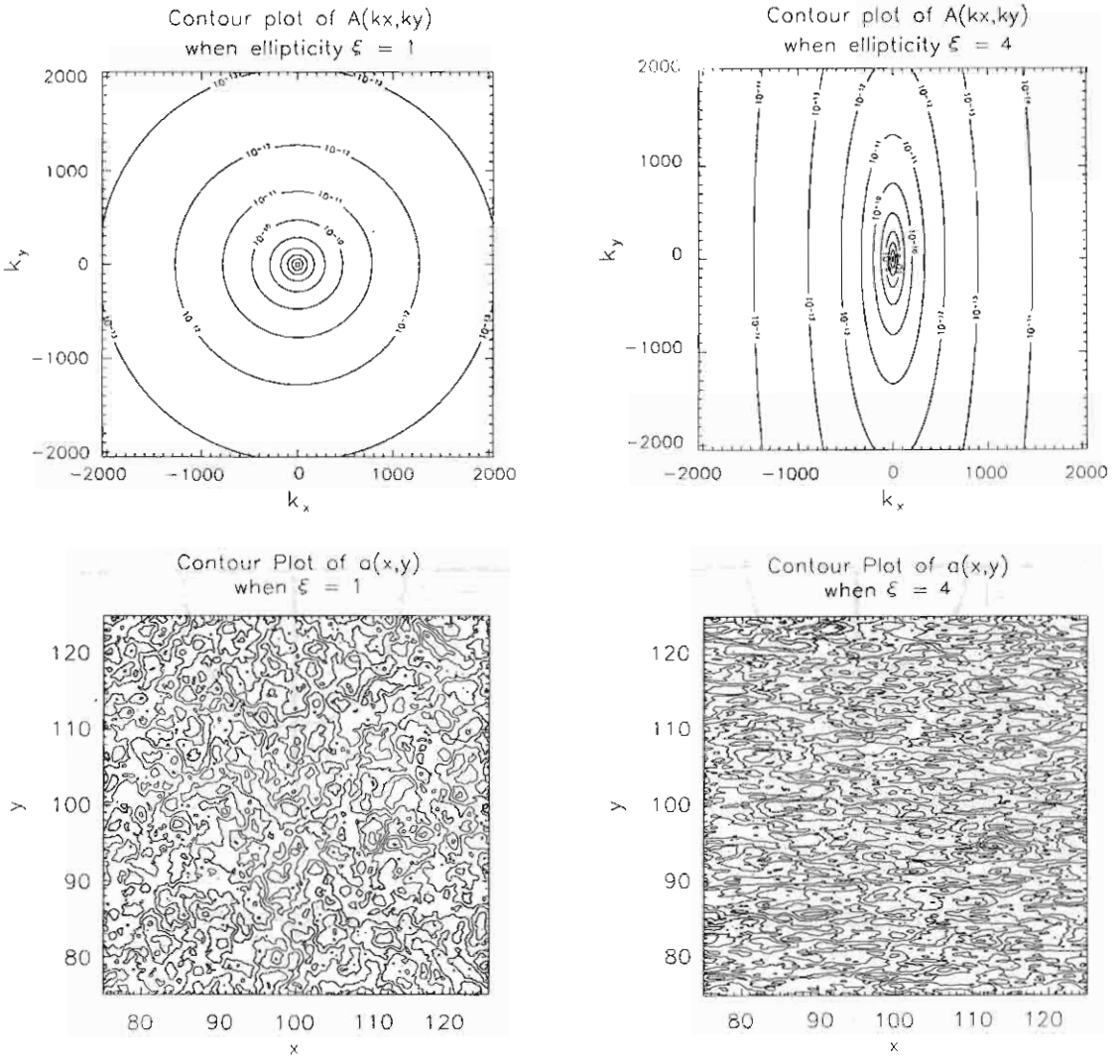

Fig. 2.— Contours of constant power $A(k_x, k_y)$ for axisymmetric ($\xi = 1$, upper left) and non-axisymmetric ($\xi = 4$, upper right) cases, and contours of corresponding representations of the potential function $a(x, y)$ ($\xi = 1$, lower left; $\xi = 4$, lower right). Note that the two-dimensional component of magnetic turbulence, $\mathbf{b}^{2D}(x, y) = \nabla \times [a(x, y)\hat{\mathbf{z}}]$, follows the contours of constant $a(x, y)$.

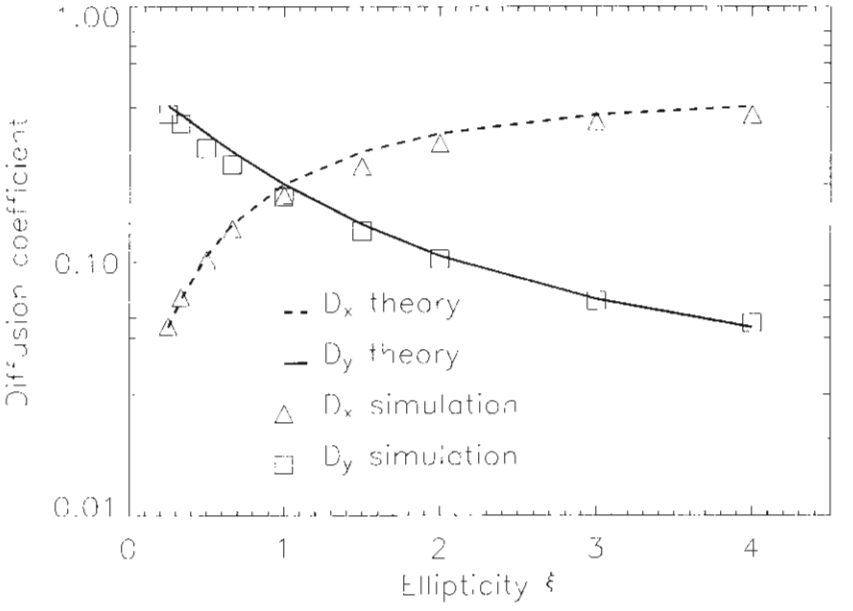

Fig. 3.— Diffusion coefficients from discrete theory and simulations for an energy ratio $E^{slab} : E^{2D} = 20 : 80$ when we vary only the ellipticity ξ (see text for details).

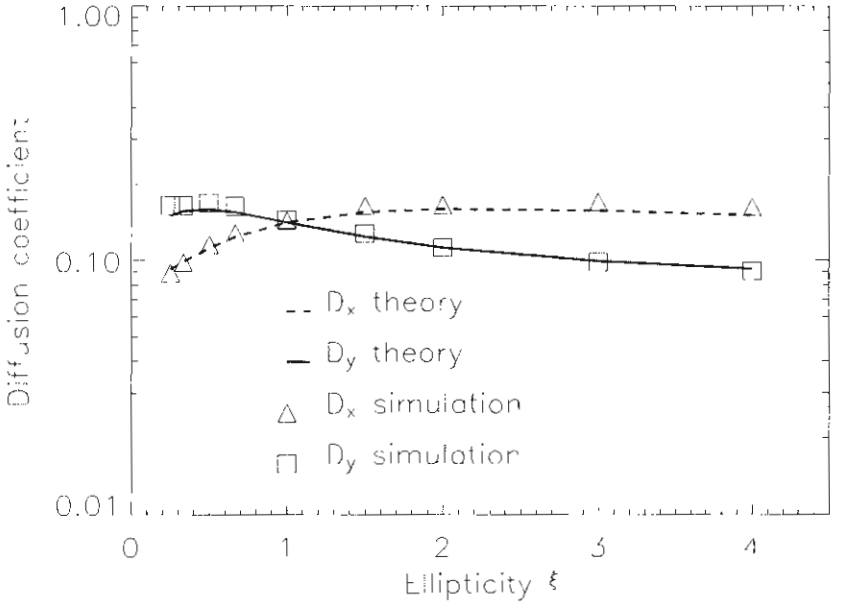

Fig. 4. – Diffusion coefficients from discrete theory and simulations for an energy ratio $E^{slab} : E^{2D} = 80 : 20$ when we vary only the ellipticity ξ (see text for details).

Table 1: Discrete theory and simulation results for the diffusion coefficients and their differences when we vary f_x, ℓ_{zx}, and ℓ_{zy}, for slab turbulence only.

Run	f_x	ℓ_{zx}	ℓ_{zy}	D_x theory	D_y theory	D_x sim.	D_y sim.	ΔD_x (%)	ΔD_y (%)
1	0.50	1.0	1.0	0.09762	0.09762	0.09591	0.09632	-1.75	-1.33
2	0.25	1.0	1.0	0.04881	0.14644	0.04879	0.14400	-0.04	-1.67
3	0.75	1.0	1.0	0.14644	0.04881	0.14859	0.04815	+1.47	-1.35
4	0.50	1.0	2.0	0.09762	0.19200	0.09717	0.19738	-0.46	+2.80
5	0.50	1.0	0.5	0.09762	0.05016	0.09989	0.04875	+2.33	-2.81
6	0.50	2.0	1.0	0.19200	0.09762	0.19011	0.09640	-0.98	-1.25
7	0.50	0.5	1.0	0.05016	0.09762	0.04941	0.09661	-1.50	-1.03
8	0.75	1.0	2.0	0.14644	0.09600	0.14338	0.09625	-2.09	+0.26